Hindawi
International Journal of Energy Research
Volume 2024, Article ID 5395508, 23 pages
https://doi.org/10.1155/2024/5395508

Research Article

Comparative Evaluation of Liquid Cooling-Based Battery Thermal Management Systems: Fin Cooling, PCM Cooling, and Intercell Cooling

Hongseok Choi, Hyoseong Lee, Ukmin Han, Juneyeol Jung, and Hoseong Lee

Department of Mechanical Engineering, Korea University, 409 Innovation Hall Bldg, Anam-dong, Seongbuk-gu, Seoul, Republic of Korea

Correspondence should be addressed to Hoseong Lee; hslee1@korea.ac.kr

Received 20 July 2023; Revised 1 April 2024; Accepted 5 April 2024; Published 20 April 2024

Academic Editor: Gianluca Coccia

The escalating demand for electric vehicles and lithium-ion batteries underscores the critical need for diverse battery thermal management systems (BTMSs) to ensure optimal battery performance. Despite this, a comprehensive comparative analysis remains absent. This study seeks to assess and compare the thermal and hydraulic performances of three prominent BTMSs: fin cooling, intercell cooling, and PCM cooling. Simulation models were meticulously developed and experimentally validated, with each system's design parameters optimized under identical volumes to ensure equitable comparisons. In the context of fast-charging conditions, intercell cooling consistently met and even surpassed the desired target temperature, reducing the maximum temperature to 30.6°C with an increasing flow rate, while fin cooling faced challenges. Effective control of coolant temperature emerged as a critical factor for achieving optimal PCM cooling, with a potential reduction in temperature difference by 4.3 K. Despite exhibiting higher power consumption, intercell cooling demonstrated the most efficient cooling effect during fast charging. Considering the BTMS weight, fin cooling exhibited the lowest energy density, approximately half that of other methods. Addressing precooling and preheating conditions for high and low temperatures, the intercell method proved adept at meeting temperature requirements with minimal power consumption in significantly shorter durations. Conversely, the practicality of using PCM at high temperatures was deemed challenging.

1. Introduction

The transition towards electric vehicles (EVs) over internal combustion engine vehicles (ICEVs) is propelled by the dual benefits of environmental sustainability and reduced oil dependency [1, 2]. Despite this trend, the transition faces hurdles, including longer charging times and safety concerns exacerbated by recent fire incidents, which underscore the need for advancements in EV technology [3].

Vital for EV performance and safety, the battery thermal management system (BTMS) regulates temperatures (15°C to 40°C) to optimize operation and extend lifespan [4, 5]. It minimizes temperature differentials, crucial for preventing power loss or accelerated degradation, and manages to keep internal temperature variations below 5 K to avert overcharging and thermal runaways, underscoring its role in enhancing EV efficiency and safety [6].

In addressing the thermal management of EVs, researchers have developed various BTMS approaches such as air cooling [7, 8], liquid cooling [9, 10], and phase change material (PCM) cooling [11, 12] to tackle the heat generated during fast charging and under extreme temperatures. While air cooling is favored for its simplicity, it falls short in high-energy-density batteries due to its low heat transfer efficiency [13]. Conversely, liquid cooling, adopted by leading EV manufacturers including Tesla, GM, and BMW, offers superior heat dissipation [9]. It encompasses direct and indirect methods, with indirect cooling predominantly utilized in BTMS, featuring fin cooling with cooling plates and fins, and intercell cooling with plates between batteries. These methods enhance cooling but face challenges in achieving uniform thermal distribution. Direct liquid cooling significantly enhances efficiency by allowing direct contact between the coolant and batteries, thereby reducing contact resistance [14]. However, this method increases system complexity, costs, and weight due to the higher volume of coolant required. The choice of BTMS thus involves a trade-off between efficiency, weight, cost, and the specific thermal management needs of EV applications [3, 15]. Despite the challenges, liquid cooling emerges as a superior solution for its enhanced cooling capacity, essential for meeting the operational demands of modern EVs. This review highlights the imperative of optimizing BTMS designs to facilitate widespread EV adoption and enhance performance across diverse operational conditions. The development and refinement of efficient BTMS solutions are crucial for overcoming existing limitations and unlocking the full potential of electric mobility.

In fin cooling, heat from the battery is transferred to the bottom cooling plate through the cooling fin inserted between the batteries. Fin cooling systems are widely used in current EVs because of the ease of manufacturing the cooling fin and bottom cooling plate. Chung and Kim [16] optimized the structure of an indirect liquid fin cooling BTMS to enhance cooling performance and thermal uniformity under quick-charge conditions. They introduced the concept of equivalent heat conductance as a key parameter for evaluating the cooling performance of the BTMS. Xie et al. [17] investigated an Al plate-assisted liquid cooling BTMS. They found that increasing the thickness of the Al plate can improve cooling performance. However, it may increase system weight. To address this issue, they proposed a cooling plate design with an appropriate Al plate thickness that could enhance the cooling performance while maintaining a weight increase of only 16.4 wt% compared to the previously reported structure.

Intercell cooling is similar to fin cooling because it employs a cooling plate. However, the cooling plates in intercell cooling are placed between the battery cells, resulting in a higher heat transfer ability compared with fin cooling, which utilizes a bottom cooling plate that indirectly contacts the batteries. Feng et al. [18] carried out the performance optimization of air/liquid coupled cooling systems to improve cooling performance and power efficiency for cylindrical batteries. With the optimized structure, only 1 $m \cdot s^{-1}$ of air and 0.2 $m \cdot s^{-1}$ of liquid could satisfy the target temperature condition even under 4C discharging condition. Gungor et al. [19] developed canopy-to-canopy cooling systems for intercell design, demonstrating that designing an appropriate flow path can yield a higher cooling performance with a lower mass flow rate. They also introduced the concept of nondimensional pumping power to evaluate the simultaneous effects of cooling and hydraulic performance.

Recently, numerous passive cooling methods have been adopted to reduce the power consumption of BTMSs, so PCM cooling has emerged as a novel thermal management system. A PCM with an appropriate melting temperature can effectively absorb a significant amount of heat from the battery, preventing it from surpassing its optimal temperature. PCM cooling utilizes the latent heat released during the phase change process, thereby reducing the power consumption of the overall system. However, the PCM has a large problem that it has low thermal conductivity, so many studies are conducted to effectively utilize the PCM for the BTMS [12, 20]. Lee et al. [21] proposed a hybrid PCM structure that combines a pouch-type PCM with a conventional fin cooling structure, enabling the practical implementation of PCMs in BTMSs. This hybrid PCM configuration exhibited superior thermal performance. The researchers emphasized the importance of considering an appropriate coolant operating strategy to effectively utilize the PCM. Singh et al. [12] developed an electrochemical-thermal model to investigate the combined BTMS of airflow and PCM encapsulation. Notably, when PCM was encapsulated as thin as 1 mm, the temperature could decrease up to 31 K under 5C discharging condition, and they introduced a compact mathematical equation to predict the temperature of the battery in advance.

Throughout the literature review, recent studies have concentrated on enhancing the thermal and hydraulic performances of various BTMSs. It has become evident that no single BTMS can be universally deemed superior, as each system possesses its own set of advantages and disadvantages depending on specific operating conditions. Moreover, there is a growing recognition of the importance of efficiently cooling and heating batteries to maintain their performance and lifespan. Recently, with the increase in battery heat generation, the use of phase change materials (PCM) has surged. However, most studies comparing BTMSs have primarily focused on air-based and liquid-based systems [22–24]. Additionally, despite extensive research on PCM, its comparisons with other BTMSs have been limited, often concentrating on the development of PCM-based BTMS without adequate evaluation against other systems [25, 26]. Moreover, many studies have introduced new BTMSs and compared them with baseline configurations [14, 21, 27]. However, there exists a possibility for the performance of these baseline structures to also be enhanced. Comparisons that fail to account for this improvement can inadvertently highlight the superiority of the proposed structures. Lastly, since electric vehicles operate across a range of temperatures, not just at room temperature but also under low and high temperature conditions, the performances of battery cooling and preheating at low temperatures must be jointly analyzed. Most studies have designed BTMSs considering only cooling or preheating performance, not both [28, 29]. Therefore, this study is aimed at comparing the thermal and hydraulic performances of three prominent BTMSs, fin cooling, intercell cooling, and PCM cooling, under conditions involving 3C charging and varying ambient temperatures. All BTMSs were optimized structurally for enhanced performance, and the efficiency of each thermal management system was compared and analyzed based on these optimized configurations.

In this study, computational fluid dynamic (CFD) simulation models were developed and experimentally validated. A 16 Ah pouch-type battery was selected for the investigation, and its heat generation under 3C charging conditions was determined and experimentally validated. Battery cooling experiments employing PCM and intercell cooling plates were conducted to refine the CFD simulation models and to compare the performance of each BTMS. Subsequently, three types of BTMSs were developed to enhance their thermal performance while maintaining the same system volume. With these improved designs, their cooling performances under 3C charging conditions were compared across various scenarios, and the heat transfer mechanisms to each component were examined. Furthermore, the power consumption and energy density requirements for each BTMS were evaluated. Lastly, the precooling and preheating performances were analyzed to ensure the effective utilization of the batteries at temperatures beyond typical operating ranges.

2. Research Approach

2.1. Design Description. In this study, three BTMSs—fin, PCM, and intercell BTMS—were selected to compare their thermal performance for a battery module with eight cells under fast-charging and preheating conditions. Fin BTMS is a liquid cooling method that is often chosen because of its simple structure and effective liquid cooling performance [30]. As shown in Figure 1(a), fins which have 3 mm thickness are attached to the surface of the battery and transfer heat from the battery to the bottom cooling plate located under the battery and fin assembly. The heat transferred to the cooling plate is eliminated by the coolant passing through the plate. In this system, the properties of the fin, such as the thickness or material, significantly affect the cooling performance; however, its thickness was fixed to match the overall size of other BTMSs. Next, a PCM-assisted hybrid fin BTMS, which was developed in our previous study, was selected. PCM is a passive cooling method that utilizes the latent heat of the PCM to suppress battery temperature increase by storing the heat generated from the batteries [21]. As shown in Figure 1(b), one surface of the battery is attached with PCM pouches which is 29.18 g per pouch and the other side is in contact with 1 mm of fins. The height of fin cooling and PCM cooling is slightly different owing to different thickness of the fin. When the battery temperature exceeds the melting point of the PCM, it starts to melt, and the PCM absorbs the heat generated from the batteries. The battery temperature is maintained at the temperature around the melting point until the PCM fully changes to the liquid state. The melting point of the PCM in this study was 36.1°C to control the battery temperature within 40°C. The thickness of the PCM pouch was chosen to be similar to those of the fin and intercell BTMSs. Finally, the intercell BTMS is chosen for BTMS performance comparison. This system has cooling plates and an ethylene-propylene-diene rubber (EPDM) sheet between the battery cells, as shown in Figure 1(c); the EPDM sheet prevents the swelling of the battery. A serpentine channel is designed inside the cooling plate, and the coolant passes through it. The flow path of the serpentine design is intentionally shaped to guide the entering coolant towards the center, where the temperature is expected to be the highest. This design is aimed at minimizing the temperature difference of the battery. When the battery generates heat, the cooling plate absorbs it at the surface of the battery, and the coolant absorbs the heat externally. Because many studies have proven that the shape of the channel affects the performance of the cooling system, such as thermal performance and power consumption, this study optimized the channel design using multiobjective optimization to improve thermal performance and decrease power consumption.

This study used a pouch-type lithium-ion nickel-manganese-cobalt (LiNiMnCo) battery (Kokam, SLPB75106205) with dimensions of 188 mm × 100 mm × 8 mm (length × width × thickness). Its nominal voltage and capacity were 3.7 V and 16 Ah, respectively, and could afford up to 3C constant current-constant voltage (CC-CV) charging experiment. C-rate represents the current-to-speed ratio at which the battery charges from 0 to 100% SOC or vice versa. The detailed specifications of the battery are listed in Table 1.

2.2. Numerical Model. In this study, we utilized the ANSYS Fluent software for the numerical analysis to obtain various results under different conditions. Several assumptions were made for the simulations, as listed below:

(i) Gravitational effects were considered in the 3D simulation [21]

(ii) A uniform heat generation model was applied for battery heat generation, and the radiation effect was neglected [9, 21]

(iii) All processes were considered transient and varied over time [9, 14, 32]

(iv) All the properties used in this study were calculated at 25°C, as listed in Table 2

(v) The coolant was assumed to be in the liquid state only, and the PCM could undergo the phase change process [21]

(vi) The Boussinesq approximation method was used for the density model of the PCM to manage the density change due to natural convection during the phase change process [33]

(vii) Boundary conditions for the numerical simulations are summarized in Table 3

The lithium-ion battery is a composite material with various layers, such as cathode, anode, electrolyte, and jelly roll. This induces nonuniform temperature distribution inside the battery, so modelling all these components is required for accurate results. However, current study utilized the lumped thermal capacity model, which assumed the battery as a uniform heat generation model, considering the Biot number (Bi). Generally, if the Biot number is less than 0.1, we can assume the lumped thermal capacity model

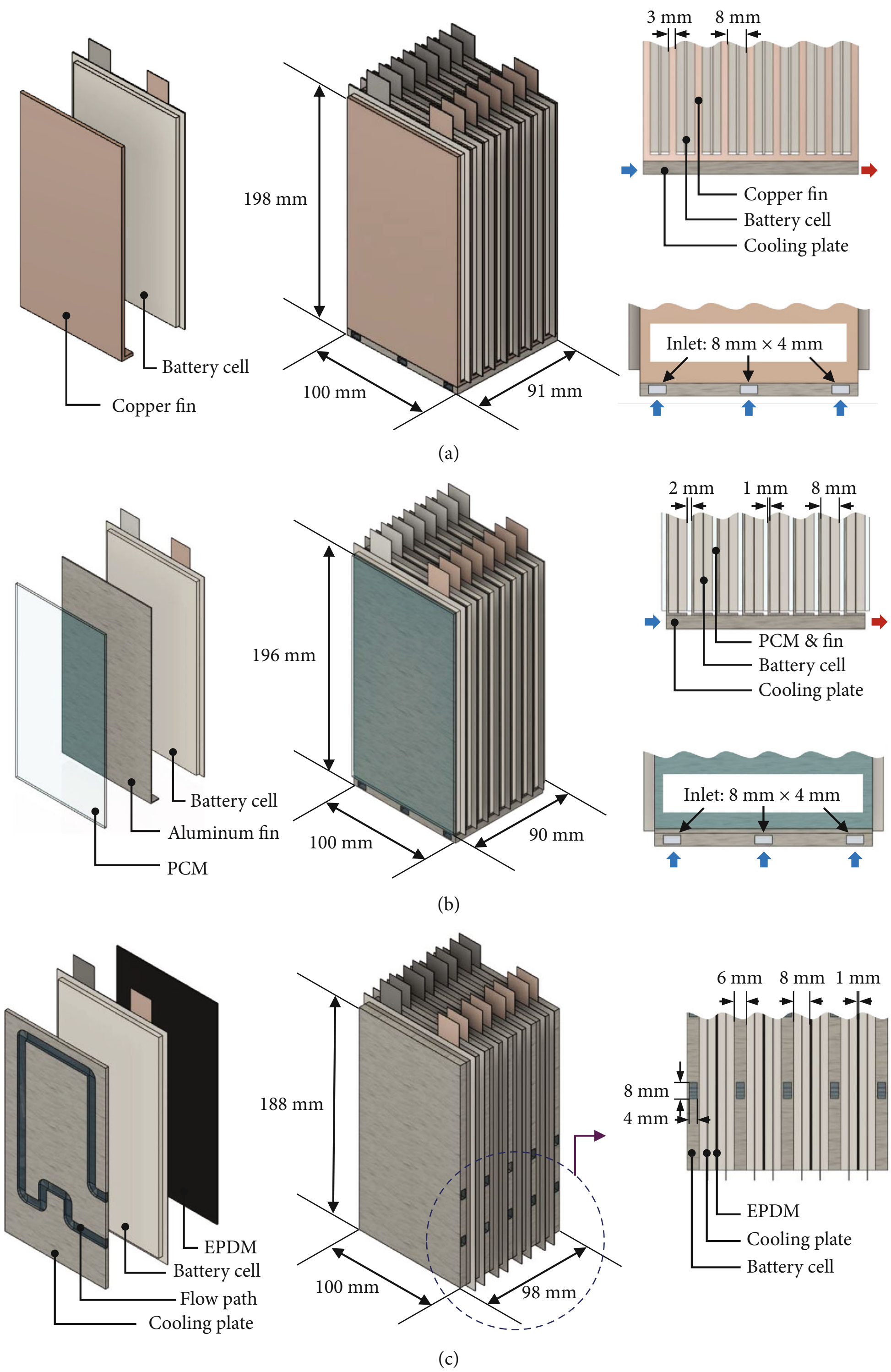

Figure 1: Detailed structures of (a) fin BTMS, (b) PCM-assisted hybrid fin BTMS, and (c) intercell BTMS.

Table 1: Specifications of the battery cell [14, 31].

Item (unit)	Value
Active material	$LiNi_{1/3}Mn_{1/3}Co_{1/3}O_2$-graphite
Electrolyte	Polymer
Nominal capacity (Ah)	16
Nominal voltage (V)	3.7
Nominal energy (Wh)	59.2
Battery energy density	
Gravimetric (Wh•kg^{-1})	179
Volumetric (Wh•L^{-1})	396
Max. charge/discharge current (A)	48
Width (mm) (x-direction)	100
Length (mm) (y-direction)	188
Thickness (mm) (z-direction)	8
Weight (g)	330
Density (kg•m^{-3})	2,250
Specific heat (J•kg^{-1}•K^{-1})	1,230
Thermal conductivity	
In-plane (W•m^{-1}•K^{-1})	26.57
Cross-plane (W•m^{-1}•K^{-1})	0.97

[35]. Therefore, the Biot number for all direction was calculated as

$$\begin{cases} \mathrm{Bi}_x = \dfrac{hL_c}{k_x} = \dfrac{2.3\times 0.1}{26.57} \approx 0.008656 < 0.1, \\ \mathrm{Bi}_y = \dfrac{hL_c}{k_y} = \dfrac{2.3\times 0.188}{26.57} \approx 0.016273 < 0.1, \\ \mathrm{Bi}_z = \dfrac{hL_c}{k_z} = \dfrac{2.3\times 0.008}{0.97} \approx 0.017848 < 0.1. \end{cases} \tag{1}$$

Bi_x, Bi_y, and Bi_z are the Biot number for x-, y-, and z-direction, respectively, and h and L_c are the convective heat transfer coefficient and characteristic length for each direction. The convective heat transfer coefficient is 2.3 W·m^{-2}·K^{-1} which is calculated using a generalized reduced gradient algorithm developed in our previous study [35]. k_x, k_x, and k_x are the x-, y-, and z-directional thermal conductivity of battery, respectively.

The principle of heat generation in the battery was analyzed to derive the exact heat generation rate during the charging process [14]. The heat generation of the battery can be expressed using

$$\dot{Q}_{\mathrm{gen}} = \dot{Q}_{\mathrm{irr}} + \dot{Q}_{\mathrm{rev}}. \tag{2}$$

$\dot{Q}_{\mathrm{gen}}$ is the overall heat generation rate and is divided into $\dot{Q}_{\mathrm{irr}}$ and $\dot{Q}_{\mathrm{rev}}$, which represent the irreversible and reversible heat, respectively.

Irreversible heat is the Joule heat caused by the internal resistance of the battery and can be expressed as the product of the current and overpotential due to the internal resistance, as shown in

$$\dot{Q}_{\mathrm{irr}} = I(V_{\mathrm{oc}} - V_{\mathrm{cell}}), \tag{3}$$

where I, V_{oc}, and V_{cell} are the current, open-circuit voltage (OCV), and battery voltage, respectively.

In contrast, the reversible heat is the heat generated by the entropy change and can be expressed by:

$$\dot{Q}_{\mathrm{rev}} = -IT\frac{dV_{\mathrm{oc}}}{dT}, \tag{4}$$

where T and dV_{oc}/dT are the temperature and the entropic coefficient of the battery, respectively. Unlike other values, the entropy coefficient cannot be directly obtained from experiments and requires a special calculation method. In this study, it was determined using an inverse heat transfer analysis method, which was developed in our previous study [35].

For the battery thermal model, the energy conservation equation for the battery is given by [9]

$$mc_{\mathrm{p}}\frac{dT}{dt} = k_x\frac{\partial^2 T}{\partial x^2} + k_y\frac{\partial^2 T}{\partial y^2} + k_z\frac{\partial^2 T}{\partial z^2} + \dot{Q}_{\mathrm{gen}} - \dot{Q}_{\mathrm{dis}}, \tag{5}$$

where m and c_{p} are the mass and specific heat.

During the battery charging/discharging process, the heat from the battery can be dissipated into the environment owing to the convection effect, which is expressed by $\dot{Q}_{\mathrm{dis}}$ as in

$$\dot{Q}_{\mathrm{dis}} = hA(T - T_{\mathrm{amb}}), \tag{6}$$

where A and T_{amb} denote the heat transfer area and ambient temperature, respectively.

The energy equation for the solid region, such as the cooling plate, is expressed in

$$\frac{\partial}{\partial t}(\rho_{\mathrm{s}} c_{\mathrm{p,s}} T_{\mathrm{s}}) = \nabla\bullet(k_{\mathrm{s}}\nabla T_{\mathrm{s}}), \tag{7}$$

where ρ_{s}, $c_{\mathrm{p,s}}$, T_{s}, and k_{s} are the density, specific heat, temperature, and thermal conductivity of the solid, respectively.

The continuity, momentum, and energy conservation equations for the fluid region are expressed in

$$\begin{gathered} \frac{\partial \rho_{\mathrm{f}}}{\partial t} + \nabla\bullet\left(\rho_{\mathrm{f}}\vec{v}_{\mathrm{f}}\right) = 0, \\ \frac{\partial}{\partial t}\left(\rho_{\mathrm{f}}\vec{v}_{\mathrm{f}}\right) + \nabla\bullet\left(\rho_{\mathrm{f}}\vec{v}_{\mathrm{f}}\right)\vec{v}_{\mathrm{f}} = -\nabla P + \rho_{\mathrm{f}}\vec{g}, \\ \frac{\partial}{\partial t}\left(\rho_{\mathrm{f}} c_{\mathrm{p,f}} T_{\mathrm{f}}\right) + \nabla\bullet\left(\rho_{\mathrm{f}} c_{\mathrm{p,f}}\vec{v}T_{\mathrm{f}}\right) = \nabla\bullet(k_{\mathrm{f}}\nabla T_{\mathrm{f}}). \end{gathered} \tag{8}$$

In the above equations, ∇P, ρ_{f}, $c_{\mathrm{p,f}}$, T_{f}, $\vec{v}_{\mathrm{f}}$, $\vec{g}$, and k_{f} are the static pressure, density, specific heat, temperature,

Table 2: Physical and thermal properties of the materials used for the BTMS [14, 21, 34].

Item (unit)	Copper	Aluminum	PCM (n-eicosane)	EPDM	Water
Density ($kg \cdot m^{-3}$)	8,978	2,719	776	1,500	998.2
Specific heat, solid ($J \cdot kg^{-1} \cdot K^{-1}$)	381	871	2,150	1,900	—
Thermal conductivity, solid ($W \cdot m^{-1} \cdot K^{-1}$)	387.6	202.4	0.425	0.29	—
Specific heat, liquid ($J \cdot kg^{-1} \cdot K^{-1}$)	—	—	2,275	—	4,182
Thermal conductivity, liquid ($W \cdot m^{-1} \cdot K^{-1}$)	—	—	0.152	—	0.6
Melting temperature (°C)	—	—	36.1	—	—
Latent heat ($J \cdot kg^{-1}$)	—	—	247,050	—	—
Volume expansion coefficient	—	—	0.0009	—	—
Viscosity ($kg \cdot m^{-1} \cdot s^{-1}$)	—	—	$5.77 \times 10^{-2} - 2.77 \times 10^{-4} T + 3.4 \times 10^{-7} T^2$	—	0.001003

Table 3: Boundary conditions for numerical simulations.

Item (unit)	Value
Charging rate (C)	3
Ambient/initial temperature (°C)	0 (preheating), 25 (cooling), 40 (precooling)
Coolant inlet temperature (°C)	25-35
Coolant mass flow rate ($g \cdot s^{-1}$)	0-20

velocity vector, gravitational vector, and thermal conductivity of the fluid, respectively.

The PCM undergoes a phase change process between the solid and liquid states; therefore, this study adopted the enthalpy-porosity method for the CFD simulation to reflect this behavior. In this method, the PCM is considered a porous region, where the porosity governs the state of the PCM. The porosity can vary between 0 and 1, representing the solid and liquid states, respectively. Therefore, this can be considered as the liquid fraction of the PCM in the mushy zone, where melting and solidification occur.

The continuity, momentum, and energy conservation equations for the PCM are given by [33]

$$\begin{aligned}
&\frac{\partial \rho_{\mathrm{PCM}}}{\partial t} + \nabla \cdot \left(\rho_{\mathrm{PCM}} \vec{v}_{\mathrm{PCM}}\right) = 0, \\
&\frac{\partial}{\partial t}\left(\rho_{\mathrm{PCM}} \vec{v}_{\mathrm{PCM}}\right) + \nabla \cdot \left(\rho_{\mathrm{PCM}} \vec{v}_{\mathrm{PCM}}\right) \vec{v}_{\mathrm{PCM}} = -\nabla P + \nabla \cdot \left(\mu_{\mathrm{PCM}} \nabla \cdot \vec{v}_{\mathrm{PCM}}\right) \\
&\qquad + \rho_{\mathrm{PCM}} \vec{g} \beta (T - T_{\mathrm{ref}}) \\
&\qquad + \vec{S}, \\
&\frac{\partial}{\partial t}(\rho_{\mathrm{PCM}} H) + \nabla \cdot \left(\rho_{\mathrm{PCM}} \vec{v}_{\mathrm{PCM}} H\right) = \nabla \cdot (k_{\mathrm{PCM}} \nabla T_{\mathrm{PCM}}).
\end{aligned} \tag{9}$$

In the above equations, ρ_{PCM}, $\vec{v}_{\mathrm{PCM}}$, μ_{PCM}, β, and T_{ref} are the density, velocity vector, dynamic viscosity, and thermal expansion coefficient of PCM and reference temperature, respectively.

$\vec{S}$ is the momentum source term related to porosity, as shown in

$$\vec{S} = \frac{(1-f)^3}{(f^3 + \varepsilon)} C_{\mathrm{mush}}, \tag{10}$$

where ε is a small constant in the denominator, which cannot be 0 and is set to 0.001. C_{mush} is the mushy zone parameter used to determine the damping properties and is set to 10^5. This term represents the velocity damping during the transition stage [25]. f is the liquid fraction calculated using

$$f = \begin{cases} 0, & \text{if } T < T_{\mathrm{s}}, \\ \dfrac{T - T_{\mathrm{s}}}{T_{\mathrm{l}} - T_{\mathrm{s}}}, & \text{if } T_{\mathrm{s}} < T < T_{\mathrm{l}}, \\ 1, & \text{if } T_{\mathrm{l}} < T. \end{cases} \tag{11}$$

H represents the enthalpy of the PCM and can be calculated using

$$\begin{aligned}
H &= h_{\mathrm{PCM,s}} + \Delta H, \\
h_{\mathrm{PCM,s}} &= h_{\mathrm{ref}} + \int_{T_{\mathrm{ref}}}^{T} c_{\mathrm{p,PCM}} dT, \\
\Delta H &= f h_{\mathrm{sl}},
\end{aligned} \tag{12}$$

where $h_{\mathrm{PCM,s}}$, ΔH, h_{ref}, T_{ref}, $c_{\mathrm{p,PCM}}$, and h_{sl} denote the sensible enthalpy, latent enthalpy, reference enthalpy, reference temperature, specific heat capacity, and latent heat of PCM, respectively.

When developing a BTMS, the hydraulic performance and reduction in the size of the BTMS are crucial to its thermal performance. The power consumption, specific power consumption, and volumetric and gravimetric energy densities of the BTMS were calculated using [14].

$$\begin{aligned}
W &= \frac{\dot{m} \Delta P}{\rho_{\mathrm{f}}}, \\
W_{\mathrm{spe}} &= \frac{W}{\mathrm{Vol}_{\mathrm{BTMS}}}, \\
\delta &= \frac{E_{\mathrm{bat}}}{\mathrm{Vol}_{\mathrm{BTMS}}}, \\
\gamma &= \frac{E_{\mathrm{bat}}}{m_{\mathrm{BTMS}}}.
\end{aligned} \tag{13}$$

In the above equations, W, W_{spe}, ΔP, E_{bat}, $\mathrm{Vol}_{\mathrm{BTMS}}$, m_{BTMS}, δ, and γ represent the power consumption, specific power consumption, pressure drop, total battery energy, volume and mass of the BTMS, and volumetric and gravimetric energy densities, respectively.

The Reynolds number was obtained with

$$\mathrm{Re} = \frac{4\dot{m}}{\pi d \mu}, \tag{14}$$

where $\dot{m}$, μ, and d are the mass flow rate, coolant viscosity, and hydraulic diameter of the flow path, respectively. The maximum mass flow rate in this study was $20\,\mathrm{g{\bullet}s^{-1}}$, which made 1,586 of the maximum Reynolds number, to adopt the laminar flow equations in the ANSYS Fluent in this study.

For the numerical analysis, ANSYS Design Modeler was used to develop a 3D simulation geometry model of the fin, hybrid fin, and intercell cooling BTMS; the geometry models were generated, as shown in Figure 1. Only the active regions were considered for the batteries to reduce the computational cost by reducing the grid number because most of the heat from the batteries came from the active region; other regions, such as tabs and films, did not account for a large portion. ANSYS Mesh was utilized to generate meshes with 3D geometries; the mesh for intercell cooling is shown in Figure 2(a). To improve calculation accuracy, the capture proximity strategy was used to create a coarse mesh for the simple region and a fine mesh for the complicated region. If the grid number of the mesh was significantly large, the calculation accuracy would increase, thereby also increasing the computational cost; however, if it was significantly small, the numerical results could not be considered reliable owing to its low accuracy. Therefore, a grid independence test was conducted to determine the proper number of grids considering both the computational cost and accuracy, as shown in Figure 2(b). An element number of 581,160 was selected as the appropriate grid number because the maximum temperature and pressure drops converged. Compared to the element numbers of 348,006 and 700,249, the differences in the maximum temperature were 0.07% and -0.14%, respectively, and the differences in the pressure drop were 0.16% and -0.03%, respectively.

2.3. Experimental Setup. To support our semiempirical battery thermal model, necessitating certain experimental data, we conducted battery charging and cooling experiments, measuring temperature, voltage, and current. The battery cycler (PEMC 50-60, PNE Solution Co., Ltd., Republic of Korea) managed charge and discharge, supplying up to 120 A current and 50 V voltage. It recorded profiles over time on a control computer. An environmental chamber (THC576, Jinsung PLT Co., Ltd., Republic of Korea) maintained a stable ambient temperature and humidity, set at 25°C and 50%, respectively, throughout the experiments.

For temperature measurements, five t-type thermocouples (TT-T-30-SLE-1000, OMEGA Engineering, United States of America) were affixed to the battery surface and recorded using a data acquisition system (DAQ) (PX1000, Yokogawa Electric Co., Ltd., Japan). The battery cooling system included a pump to control coolant flow rate, a flow meter, RTD sensors for fluid temperatures, an external chiller for maintaining coolant temperature (-25°C to 100°C), and a heat exchanger connecting the coolant cycle with the external chiller. The chiller's inlet temperature ranged from -25°C to 100°C and the pump facilitated a flow of up to 42.8 ml per sec. RTD temperature data and mass flow rate information were saved in the DAQ. See Table 4 for the specifications and measurement accuracies of the experimental components.

To validate the simulation of cooling using the PCM and cooling plate, a PCM pouch and an intercell cooling plate were produced, as shown in Figure 3. The PCM pouch was produced by melting an n-eicosane PCM in ambient air (40°C) because it has a melting temperature of 36.1°C. The liquid-state PCM was then placed and sealed into the polyethylene pouch. Subsequently, the pouch was laid on the battery surface and was resolidified in ambient air (25°C). For the intercell cooling plate, symmetric plates with a serpentine-shaped flow path were manufactured using copper, and pipes for the inlet and outlet were inserted facing the symmetric plane of the plates. The edges of the contact surfaces of the cooling plates were welded to prevent leakage.

Data obtained by experimental equipment had measurement accuracy as listed in Table 4, resulting in errors. Therefore, the uncertainty analysis of the measured and calculated parameters was conducted. The total error consists of a system error due to the measurement limit of the equipment and a random error caused by an unexpected variable in the experiment. Among them, the random error could be reduced by conducting numerous steady experiments, but the heat generation of the battery changed over time, so it could not always be maintained the same, so only the system error was analyzed.

The calculated parameters were functions of measured parameters as shown in Eq. (15) because they were calculated using numerical equations, and the uncertainty of the calculated parameters could be obtained with Eq. (16) [9].

$$R = R(x_1, x_2, \cdots, x_n), \tag{15}$$

$$\delta R = \sqrt{\sum_{i=1}^{n}\left(\frac{\partial R}{\partial x_i}\delta x_i\right)^2} = \sqrt{\left(\frac{\partial R}{\partial x_1}\delta x_1\right)^2 + \left(\frac{\partial R}{\partial x_2}\delta x_2\right)^2 + \cdots + \left(\frac{\partial R}{\partial x_n}\delta x_n\right)^2}, \tag{16}$$

where R and δR are the calculated parameters and its uncertainty and δx_1, δx_2, $\cdots$, and δx_n are the uncertainties of the measured parameters. With these equations, the uncertainty analysis was conducted, and the results are summarized in Table 5. The uncertainty of each parameter would be calculated for every time step because the battery charging was transient process, but the values at the end of the charging were presented.

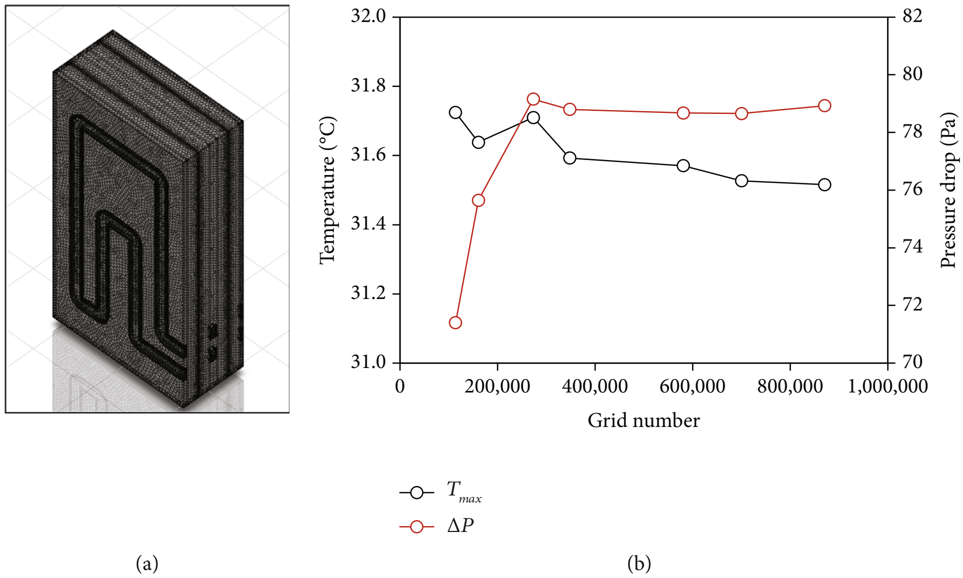

Figure 2: (a) Generated mesh and (b) grid independence test.

Table 4: Specifications of the experimental equipment and measurement accuracy.

Equipment	Manufacturer	Model	Operating range	Accuracy (F.S)
Battery cycler	PNE Solution	PEMC 50-60	0-50 V	±0.05 V
			0-120 A	±0.12 A
Environmental chamber	Jinsung PLT	THC576	-20–80°C	±0.5°C
Thermocouple	OMEGA Engineering	TT-T-30-SLE-1000	-50–200°C	±0.5°C

3. BTMS Design Validation and Development

The battery charging experiments were conducted to obtain the battery voltage, OCV, current, battery temperature, ambient temperature, and heat transfer coefficient during 3C charging to calculate the battery heat generation using Eq. (1). First, the battery cell was fully discharged to 0% SOC to measure the open-circuit voltage of the battery under 25°C of initial and ambient temperature. It was then measured from 0% to 100% at 5% SOC intervals; 21 SOC data were linearized and used to calculate the battery heat generation. Subsequently, five TCs were attached to the battery surface to measure the temperature of the battery, and another TC was used to measure the ambient temperature. The battery was completely discharged to 0% SOC and charged in 3C CC-CV mode; the data necessary for the calculation of the heat generation amount were measured. Finally, the heat transfer and entropy coefficients during battery charging were obtained using the inverse heat transfer method in a previous study [36], and the simulation temperature was compared with the experimental results under the same conditions. For the case without cooling (Figure 4), the average values of the experimental and numerical results from the same points were compared, showing a maximum error of 3.3%; therefore, battery heat generation was considered to be valid. Subsequently, the battery cooling experiments using the PCM and intercell structures under 3C charging condition were conducted to develop battery cooling simulation models under the same conditions as the battery charging experiment. As shown in Figure 3, the PCM cooling experiment involved attaching a PCM pouch to a battery cell and charging the battery at 0% SOC. The intercell cooling experiment maintained the same initial and ambient temperatures and was conducted at a mass flow rate of 10 g•s^{-1} and an inlet temperature of 25°C. The graphs in Figure 4 show the experimental and numerical results obtained for both structures, which exhibit a maximum error of 3.1%.

Three types of cooling structures were developed to improve the thermal performance of the battery, fin cooling, PCM cooling, and intercell cooling, which were designed to have similar volumes; the results under 3C charging condition for fin cooling and PCM cooling are shown in Figure 5. Generally, aluminum is used for cooling fins, and thicker cooling fins have better cooling performance because they can absorb more heat from the battery. However, in this study, copper was selected as the cooling fin material because of its higher thermal conductivity than that of aluminum. The maximum temperature and temperature difference concerning different fin thicknesses are shown in Figures 5(a) and 5(b), respectively. The coolant used was water, and the mass flow rate was 10 g•s^{-1} with an inlet temperature of 25°C. Although both cooling performances improved with increasing thickness, a fin thickness of 3 mm was selected to satisfy the battery size requirements.

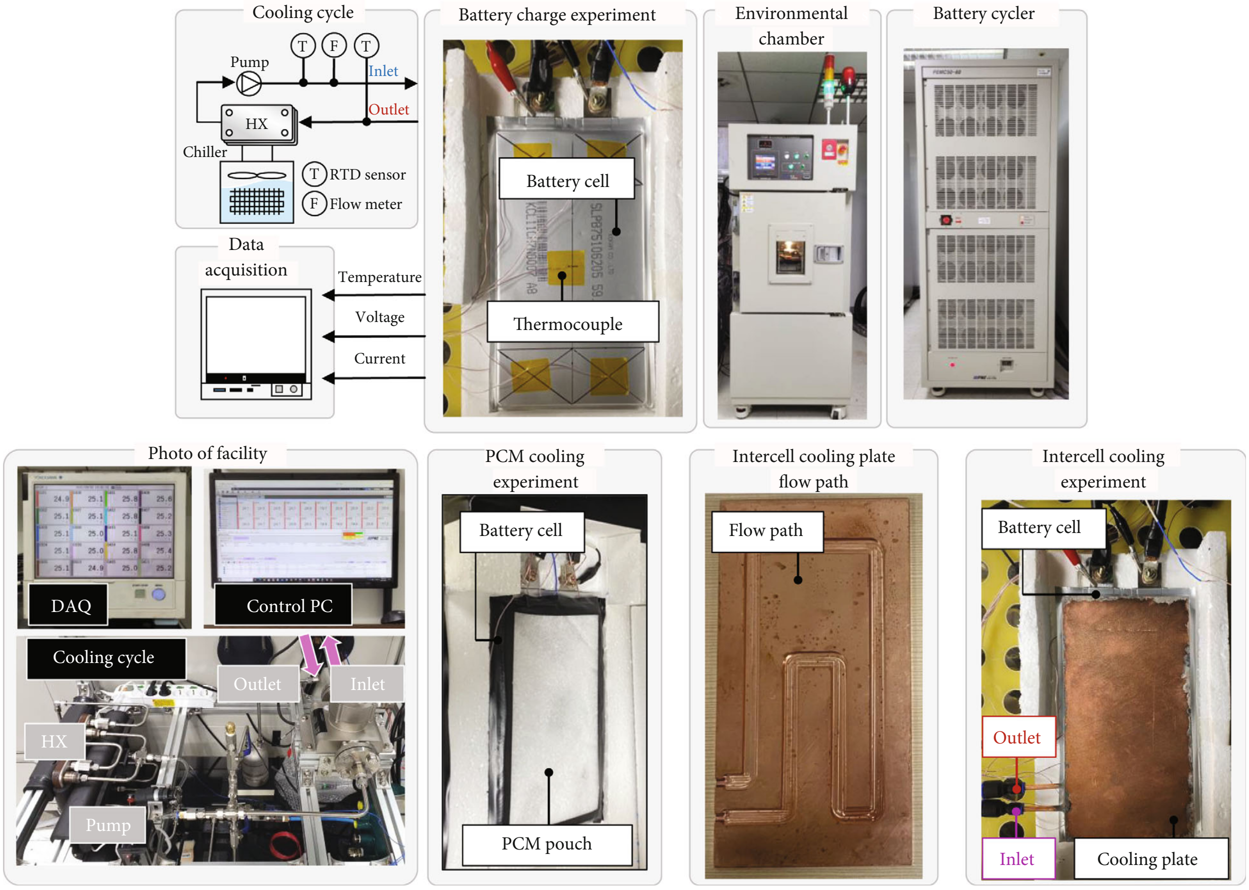

Figure 3: Experimental facilities for the battery experiments and photographs of battery cooling experiments.

Table 5: Uncertainty analysis.

Parameter	Unit	Value	Overall uncertainty
Measured parameter			
Temperature ($T_{battery}$)	°C	41.9	±0.5
Battery voltage (V_{cell})	V	4.20	±0.05
Open-circuit voltage (V_{oc})	V	4.13	±0.05
Current (I)	A	11.15	±0.12
Calculated parameter			
Average temperature (T)	°C	41.9	±0.144
Irreversible heat ($\dot{Q}_{irr}$)	W	172.1	±1.945
Reversible heat ($\dot{Q}_{rev}$)	W	-0.77	±0.789
Total heat generation ($\dot{Q}_{gen}$)	W	171.3	±2.09

The PCM cooling structure contained a 1 mm aluminum cooling fin to transfer heat to the bottom cooling plate, and the cooling performances with various PCM thicknesses are shown in Figures 5(c) and 5(d). The PCM cooling structure selected lighter aluminum rather than copper because lower conductivity of aluminum can be compensated with the PCM. The mass flow was similar, but the inlet temperature was 31°C, which was chosen as the optimal inlet temperature in our previous study [21]. Approximately 400 s after battery charging began, the maximum temperature and temperature difference started to stabilize because the PCM began to melt. Subsequently, they increased again when the PCM fully melted for the cases with 0.5 mm and 1 mm thickness. Conversely, thicker PCM showed a continuously steady trend until the end of the charging process. Therefore, a 2 mm thick PCM can provide sufficient latent heat for our battery thermal management systems while maintaining a similar volumetric size.

The intercell cooling performance was highly affected by the design of the intercell cooling plate. In this study, a serpentine design was used for the intercell cooling plate, as shown in Figure 6(a), which was optimized to improve thermal and hydraulic performances by reducing the temperature difference and pressure drop. The design variables of the cooling plate are summarized in Table 6, and the optimized processes were performed using the same cooling plate size. Based on the DOE of 160 samples and the OAAO method, a meta model was developed to predict the optimized design. Among the several types of meta models, genetic aggregation was utilized for prediction accuracy because it derives the most suitable prediction model through a genetic algorithm [37]. The battery was charged under 3C, and the mass flow rate was 10 g•s^{-1}. After developing the meta model, 25 random verification points were generated for validation. Validation was conducted for the

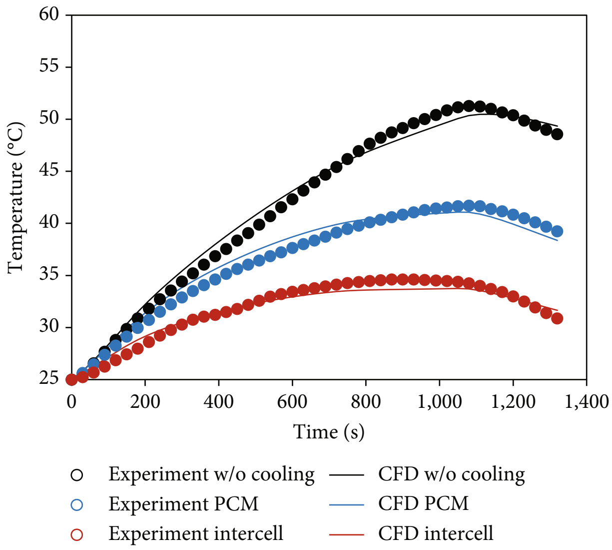

Figure 4: Simulation model validations with experimental results.

temperature difference and pressure drop and was completed with an error within 5%. With the optimization processes in the appendix, the Pareto solutions were obtained, as shown in Figure 7. The design constraint region is colored green, where both performances are better than the baseline. The final optimized intercell cooling plate design, which could reduce both the pressure drop and temperature difference, was developed (Figure 6(b)). The optimized design reduced the temperature difference and pressure drop by 19.9% and 19.2%, respectively, compared to the initial design.

4. Performance of the BTMS

4.1. Effect of Mass Flow Rate. The BTMS cooling performances of the three validated and developed simulation models were compared with respect to the mass flow rate. All the simulations were conducted under 3C charging condition, and the inlet mass flow rate was varied from 0 to 20 $g{\cdot}s^{-1}$ with 25°C inlet temperature. Initially, fin cooling did not meet the optimal battery temperature conditions, set at a maximum temperature of 40°C and a temperature difference of 5 K under the given mass flow rate conditions, as shown in Figures 8(a) and 8(d). Despite an increase in the mass flow rate, only a marginal reduction of 1.7°C in the maximum temperature was achieved when the flow rate increased from 5 to 20 $g{\cdot}s^{-1}$. The temperature difference in the battery module even increased with a higher mass flow rate of the coolant, highlighting the limitations of the fin cooling structure. The structure struggled to remove heat from the battery efficiently, resulting in a continuous increase in battery temperature, especially in the upper section far from the bottom cooling plate, as shown in Figure 9(a), which illustrated the temperature contour of the middle section of the battery. This led to a higher maximum temperature and temperature differences inside the battery.

PCM cooling could provide sufficient cooling to satisfy the maximum temperature at every mass flow rate; however, the temperature difference exceeded 5 K when the coolant flowed, as shown in Figures 8(b) and 8(e). Notably, the maximum temperature and temperature difference of PCM cooling exhibited a similar trend to that of fin cooling when the PCM was in the solid state. However, they stabilized after 400 s from the battery charging condition when the PCM started to melt. The maximum temperature remained relatively constant across all mass flow rates until approximately 900 s. After this point, the cases with 0 and 5 $g{\bullet}s^{-1}$ began to increase, indicating that the PCM had completely melted and no longer functioned as a heat storage system. Instead, it behaved similarly to a fin with a lower thermal conductivity. Therefore, the cases with a higher mass flow rate than 10 $g{\bullet}s^{-1}$ showed similar maximum temperatures because PCM restricted the batteries from being heated more due to its heat storage ability. Regarding the temperature difference, it was more uniform when the pump was not operational. As the pump begins to operate, the temperature difference of the battery increased with increasing flow rates until the PCM was completely melted. The PCM cooling method exhibits a trend similar to the fin cooling system, using a bottom cooling plate, where the temperature deviation increased as the flow rate increased. This phenomenon was due to the PCM structure, where the lower part of the battery near the cooling plate experienced a temperature decrease as the flow rate increased owing to the use of a lower cooling plate. However, the maximum temperature of the upper part of the battery, which was far from the cooling plate, was limited by the PCM. Therefore, the temperature deviation of the battery increased as the flow rate increased as illustrated in Figure 9(b).

Finally, in the case of the intercell cooling method, the maximum temperature was initially significantly high, exhibiting a small temperature difference when the pump did not work. This was also observed in the case where the pump did not operate in the fin cooling structure, resulting in an overall high temperature. However, when the flow rate started to increase, the target battery temperature conditions were consistently met. Moreover, as the flow rate continued to increase, the maximum temperature decreased by 3.2°C, from 33.8°C to 30.6°C. Compared with other methods, the intercell cooling method demonstrated a greater reduction in the maximum battery temperature owing to the increased flow rate. Additionally, the temperature difference of the battery decreased with increasing flow rate, thereby improving temperature uniformity. The temperature contour in Figure 9(c) indicated that the intercell cooling method provided a clear advantage over using a lower cooling plate by evenly cooling the battery module. Previous cooling methods relied on heat transfer through fins or PCM to the lower cooling plate, resulting in limited and unbalanced heat dissipation depending on the location of the battery, thereby leading to temperature differences. In contrast, with the intercell cooling method, all parts of the battery made direct contact with the cooling plate, thereby shortening the path for heat transfer and providing overall even cooling.

The heat generated by the batteries was absorbed by various components, including the battery itself, PCM, fin, and cooling plate, and then dissipated by the coolant.

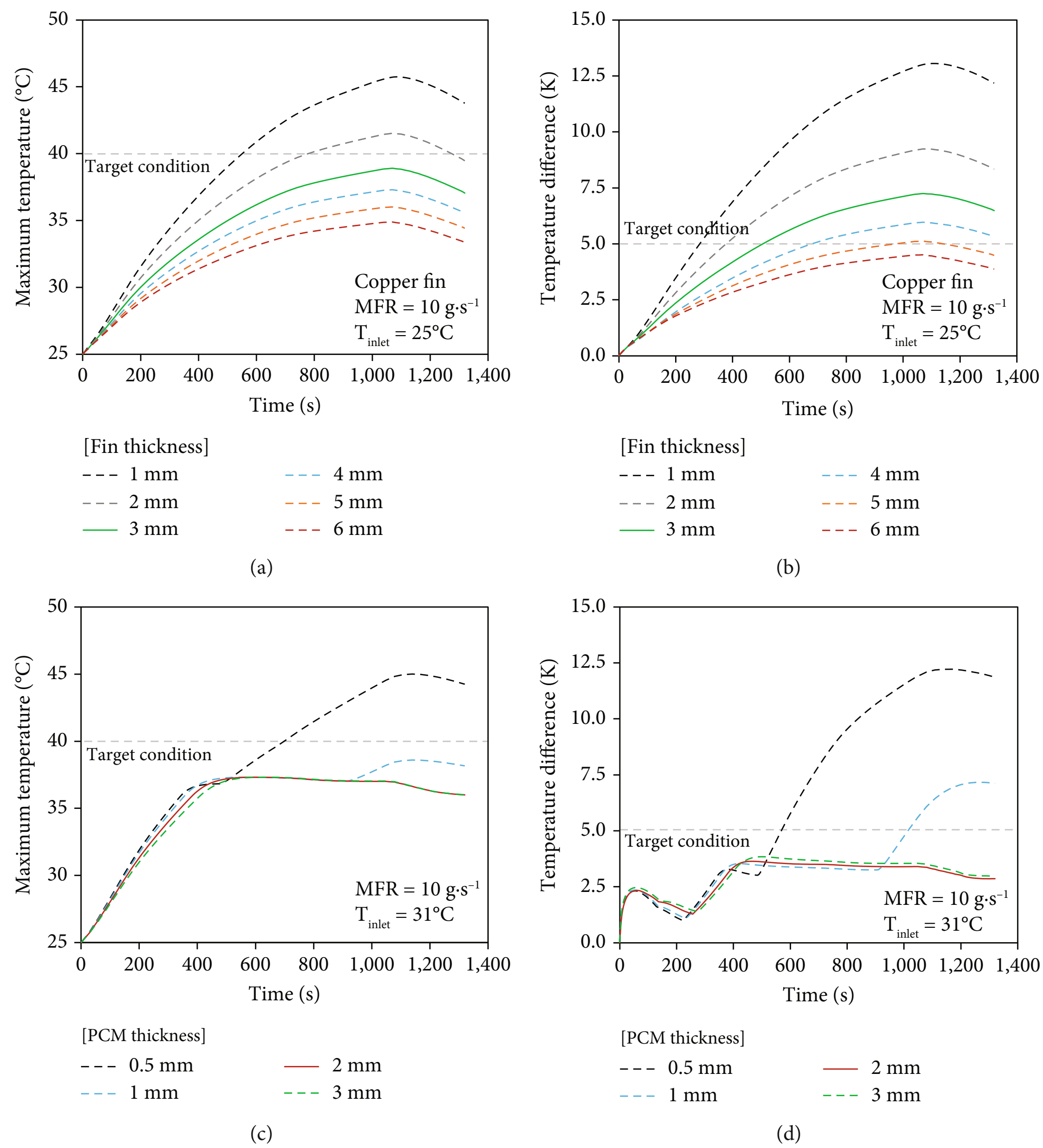

FIGURE 5: Temperature profiles concerning different thicknesses of copper fin: (a) maximum temperature ($T_{inlet} = 25^{\circ}C$), (b) temperature difference and PCM pouch ($T_{inlet} = 25^{\circ}C$), (c) maximum temperature ($T_{inlet} = 31^{\circ}C$), and (d) temperature difference ($T_{inlet} = 31^{\circ}C$).

The contribution of each component is illustrated in Figures 10(a)–10(c) under 3C charging and a mass flow rate of $10\,g{\bullet}s^{-1}$. Although fin cooling and PCM cooling shared a similar structure, PCM cooling absorbed more heat from the battery than fin cooling. However, the heat dissipated by the coolant was lower in PCM cooling before the PCM started to melt. This occurred because the solid PCM had poor thermal conductivity, whereas the copper fin exhibited superior thermal conductivity, enabling more effective heat transfer from the battery to the coolant in fin cooling than in PCM cooling. Liquid PCM also had a low thermal conductivity, resulting in inadequate heat dissipation by the coolant. Nevertheless, PCM could absorb heat through phase changes, thereby reducing the amount of heat remaining in the battery. The heat remaining in the battery became negative after 700 s, thereby decreasing the battery temperature. Intercell cooling, with its larger heat transfer area and shorter heat transfer distance between the battery and coolant, dissipated heat more effectively than the other BTMSs. Consequently, the battery absorbed less heat, leading to better thermal performance, as shown in Figure 8.

Figure 10(d) summarizes the overall heat dissipation during 3C charging. The remaining heat in the battery followed the order of fin cooling, PCM cooling, and intercell cooling, and the corresponding battery temperatures aligned with this order. Moreover, the coolant in fin cooling could remove more heat than that in PCM cooling due to the difference in thermal conductivity between the components. Although copper had a higher thermal conductivity than aluminum, it had a lower specific heat. Therefore, the heat absorbed by the fin itself was lower, and the heat absorbed by other components containing fins was also lower than those in the other cooling methods. These results indicated

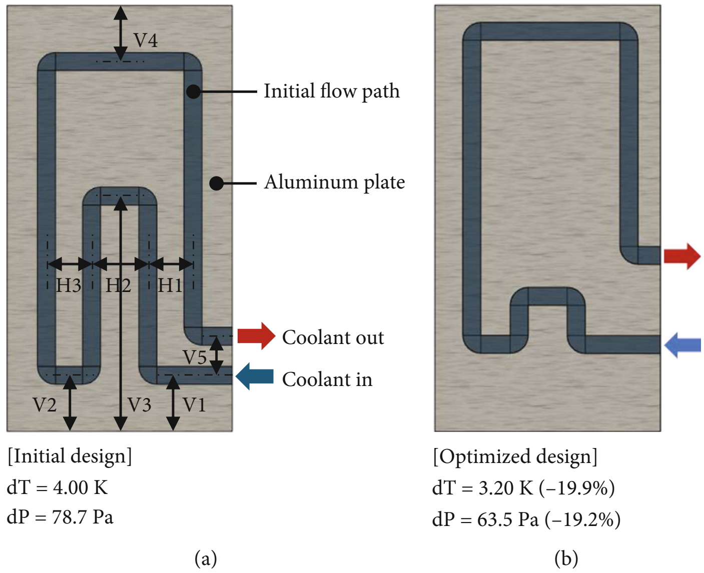

FIGURE 6: (a) Initial cooling plate design with its design parameters and (b) final optimized design.

TABLE 6: Initial and optimized values of the input parameters and their ranges with the progress of OAAO.

Step	V1 (mm)	V2 (mm)	V3 (mm)	V4 (mm)	V5 (mm)	H1 (mm)	H2 (mm)	H3 (mm)
Initial	25	25	105	25	17.5	20	25	20
1st range	10-40	10-40	60-150	10-25	15-40	15-25	15-35	15-25
2nd range	38-40	38.5-40	60-150	10-25	38-40	20-25	15-28	15-25
3rd range	38-40	38.8-40	60-150	10-20	38-40	21-25	15-28	15-25
Optimal	39.25	39.08	60.69	12.79	39.83	22.89	24.17	16.02

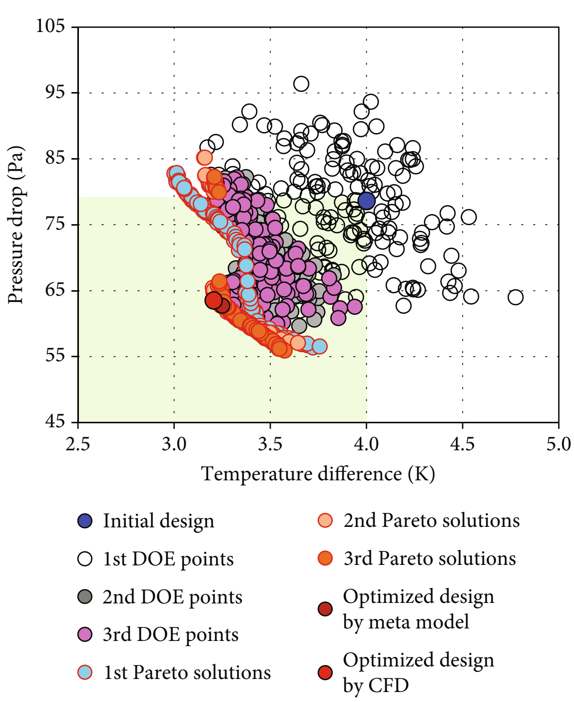

FIGURE 7: Pareto solutions.

that the cooling performance of the active system itself was low because it is aimed at assisting in dissipating the heat stored in the passive system rather than to function independently, as in the case of using the active system alone. Additionally, considering materials with high specific heat for BTMS components was crucial for improving battery heat dissipation, as the heat absorbed by these components should not be disregarded.

4.2. Effect of Inlet Temperature. The issue with using fin and PCM cooling with the bottom cooling method as the active cooling method was that the lower part of the battery that passed through the coolant was colder than the upper part. To address this concern, simulations were performed by increasing the inlet temperature of the cooling water (Figure 11). The flow rate was fixed at 10 g•s^{-1}, and the inlet temperature of the fluid was changed from 25 to 35°C, while other boundary conditions remained consistent. Analysis based on the maximum battery temperature revealed that fin and intercell cooling increased as the fluid inlet temperature rose, whereas the maximum temperature using PCM cooling remained nearly constant regardless of the fluid inlet temperature.

For fin cooling and intercell cooling BTMSs, active cooling by the bottom cooling plate significantly influenced the thermal management system's performance, making it

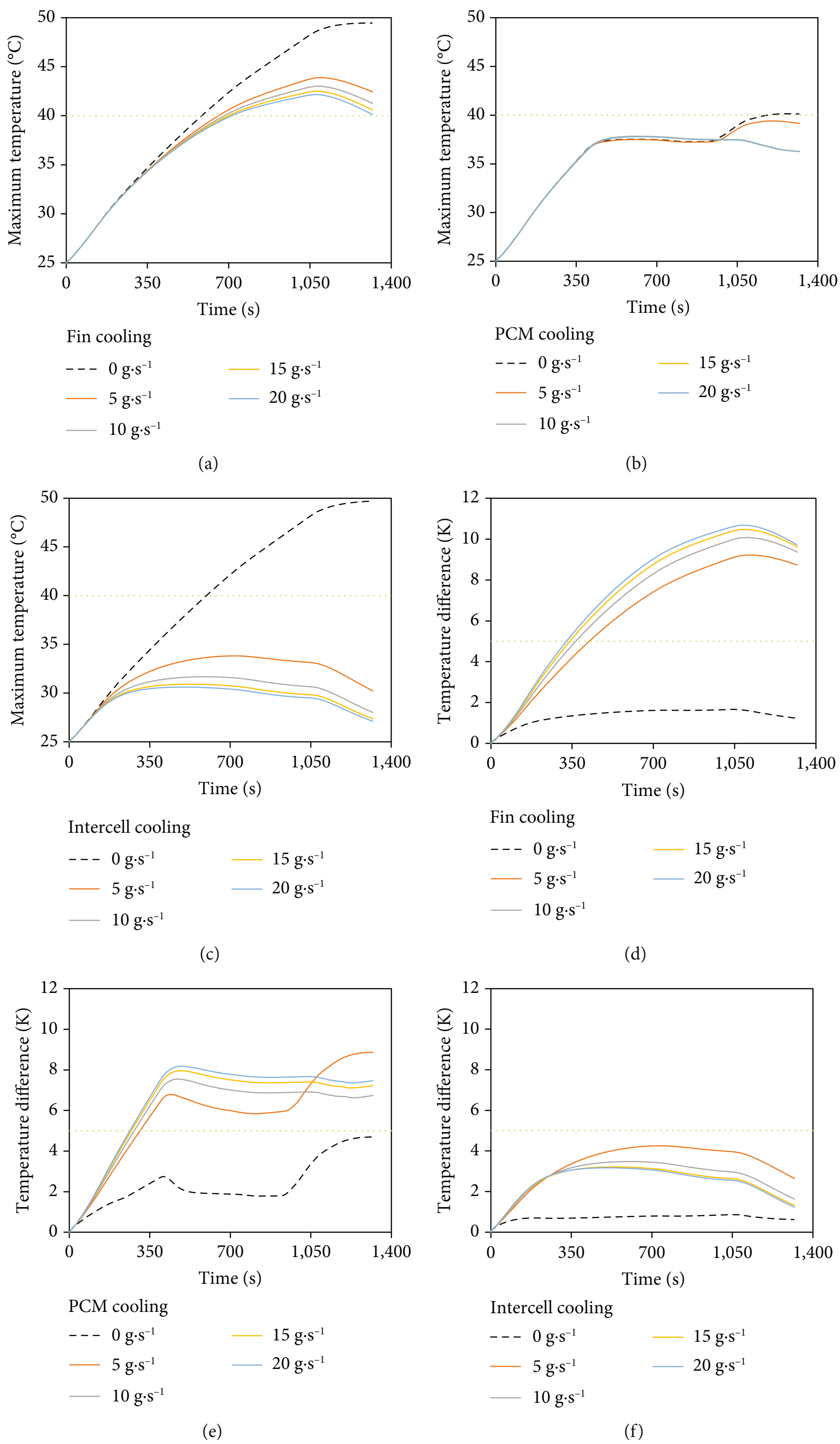

Figure 8: Maximum temperature of (a) fin, (b) PCM, and (c) intercell BTMSs; temperature difference of (d) fin, (e) PCM, and (f) intercell BTMSs concerning different mass flow rates during 3C charging condition.

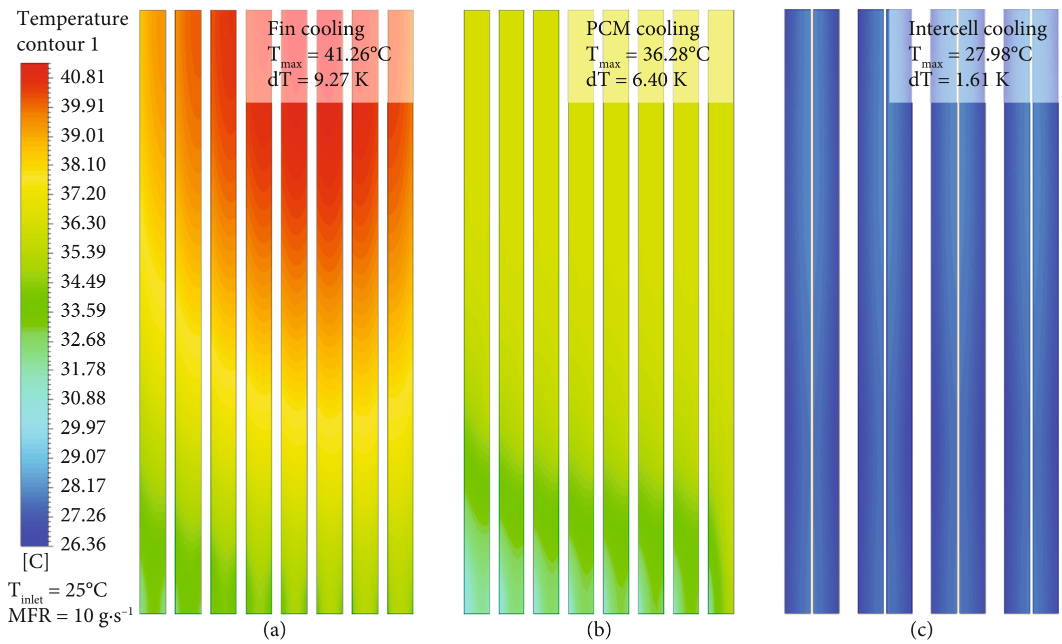

Figure 9: Temperature contours inside (a) fin, (b) PCM, and (c) intercell BTMSs.

highly sensitive to the coolant temperature. A 10°C increase in the coolant inlet temperature led to a 5.1°C and 9.2°C rise in the maximum temperature for fin cooling and intercell cooling, respectively, indicating greater sensitivity in intercell cooling due to its dependence on the coolant's temperature. In contrast, the fin could be considered a passive cooling aid to some extent. In the case of PCM cooling, the PCM contributed to passive cooling due to its robust heat storage capacity, limiting the maximum battery temperature because the PCM did not completely melt. However, if the PCM fully melted, the maximum temperature of the battery would increase, similar to the fin cooling method.

The temperature difference in the battery underwent three stages, as shown in Figures 11(d)–11(f). Initially, it rapidly increased as the battery began to charge, with a more pronounced effect observed as the coolant inlet temperature increased. Subsequently, the temperature difference decreased until the battery temperature approached the inlet temperature. The lowest temperature region of the battery typically coincided with the coolant inlet when the initial and inlet temperatures were similar, as shown in Figure 9. However, with an increase in the inlet temperature, this region experienced the highest temperature briefly at the beginning of battery charging, resulting in a reduced temperature difference, as shown in Figure 12. The temperature difference then began to increase again when the battery temperature surpassed the coolant inlet temperature, following patterns similar to those in the previous results in Figure 8.

Throughout the battery charging process, the temperature difference appeared to decrease with a higher inlet temperature owing to the increased lowest temperature. However, the fin cooling method failed to satisfy the target temperature conditions regardless of the inlet temperature, making it unsuitable for this study. As the inlet temperature increased, PCM cooling exhibited a similar maximum temperature but effectively reduced the temperature difference. Thus, controlling the inlet temperature, such as selecting an optimal temperature or modifying the temperature at which the PCM began to melt, could be crucial for utilizing PCM cooling.

Finally, the temperature difference with intercell cooling marginally decreased as the inlet temperature increased; however, the maximum temperature showed a significant increase, indicating that a lower inlet temperature was favorable for intercell cooling. PCM cooling required an inlet temperature above 29°C, whereas intercell cooling only needed it to be below 33°C. Therefore, in terms of controlling the coolant inlet temperature to meet the target battery temperature conditions, the intercell cooling method had a significant advantage.

4.3. Power Consumption and Energy Density. Building on the preceding results, increasing the coolant's mass flow rate enhances the BTMS's performance, enabling effective cooling even in less efficient air-cooled systems. However, higher mass flow rates lead to a significant increase in pressure drop and power consumption, necessitating a balance between thermal and hydraulic performances in BTMS design.

This section evaluates the specific power consumption of three BTMS types. The power consumption per BTMS volume at various flow rates during 3C charging is shown in Figure 13(a). Despite all cooling plates having the same inlet shape, the bottom cooling plate, with its straightforward flow path design, incurs relatively lower power consumption. Fin cooling and PCM cooling have similar specific power consumptions due to identical cooling plate designs. In contrast, the serpentine flow path of the intercell cooling plate leads to increased pressure drop and, thus, higher power consumption.

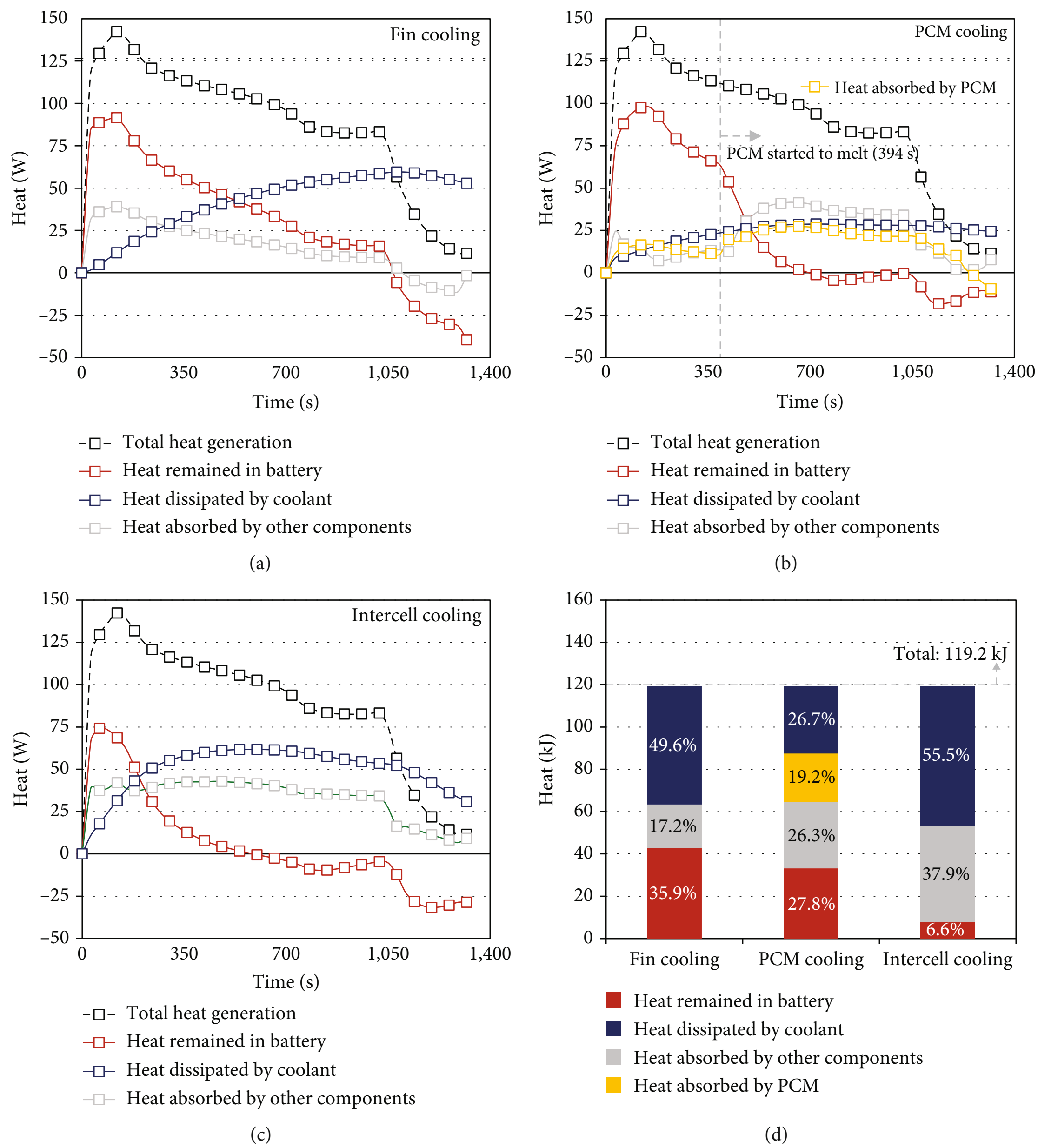

Figure 10: Heat dissipation contribution of (a) fin cooling, (b) PCM cooling, and (c) intercell cooling with respect to time and (d) overall heat dissipation results.

While intercell cooling offers superior thermal performance, its higher power demand may affect hydraulic efficiency.

Moreover, as the total weight of electric vehicles increases, their mileage decreases [32]. Thus, designing a BTMS that minimizes volume and weight is beneficial. In this study, three BTMS types with similar volumes were designed, resulting in comparable volumetric energy densities, as shown in Figure 13(b). Different cooling methods and materials led to varied gravimetric energy densities. Specifically, fin cooling, using copper, exhibited almost half the gravimetric energy density of other methods due to copper's higher density compared to aluminum. PCM cooling, using materials with lower density than metals, achieved the highest gravimetric energy density. The intercell method, using aluminum plates, is lighter than fin cooling but does not reach PCM cooling's gravimetric efficiency. Therefore, PCM cooling emerges as the most efficient BTMS in terms of gravimetric energy density, potentially enhancing electric vehicle mileage.

4.4. Precooling and Preheating Performance. Maintaining a battery's operating temperature within the 15-40°C range is universally recognized as crucial for optimal performance. Predominantly, research has focused on battery operation at an optimal temperature of 25°C. Temperature increases, typically observed during charging and discharging processes, can precipitate thermal runaway if the battery pack's internal temperature continues to rise without adequate heat dissipation. Moreover, for every 1°C increase within the 30-40°C range, battery lifespan diminishes by roughly two months

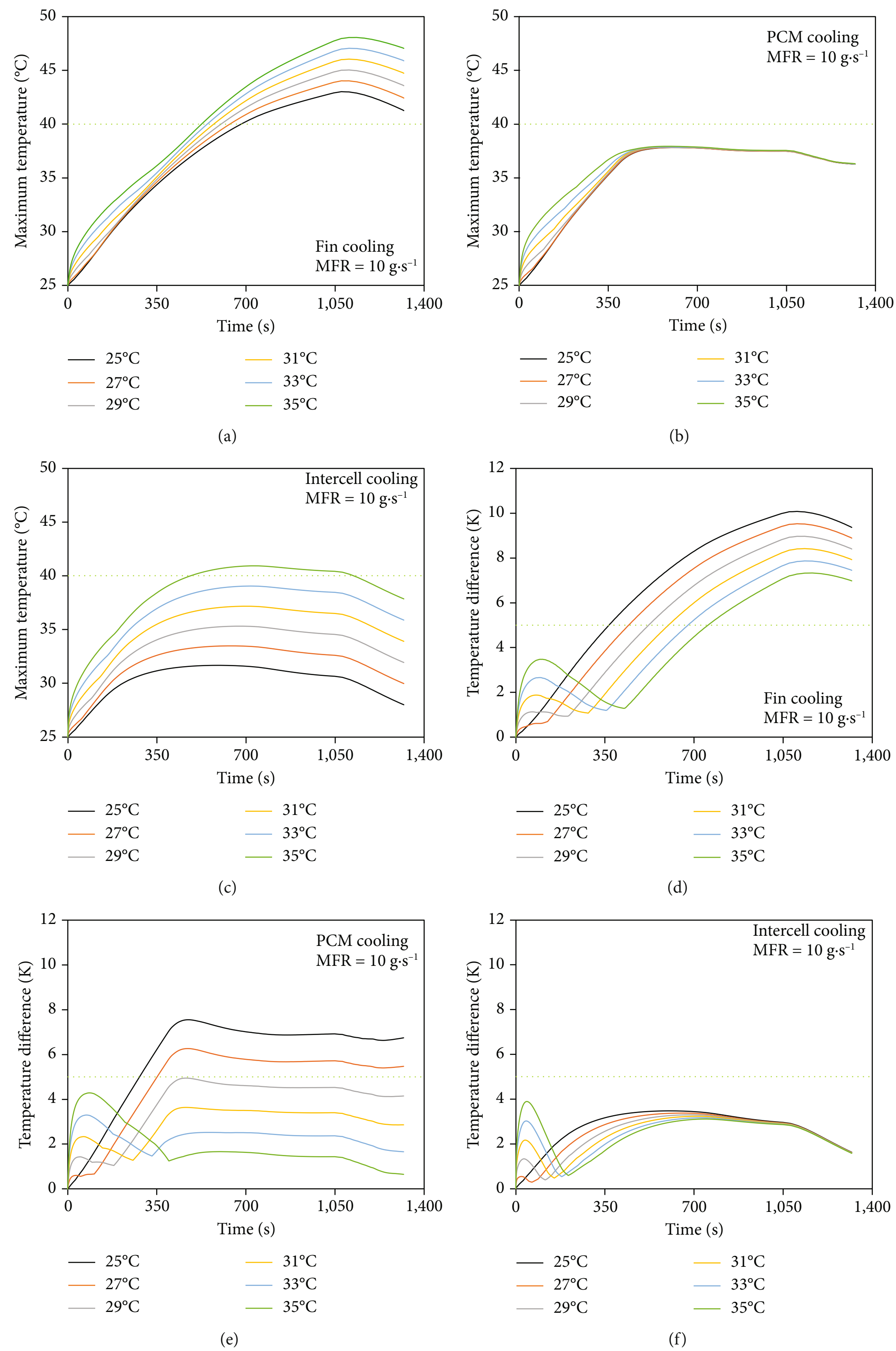

FIGURE 11: Maximum temperature of (a) fin, (b) PCM, and (c) intercell BTMSs and temperature difference of (d) fin, (e) PCM, and (f) intercell BTMSs concerning different inlet temperatures during 3C charging condition.

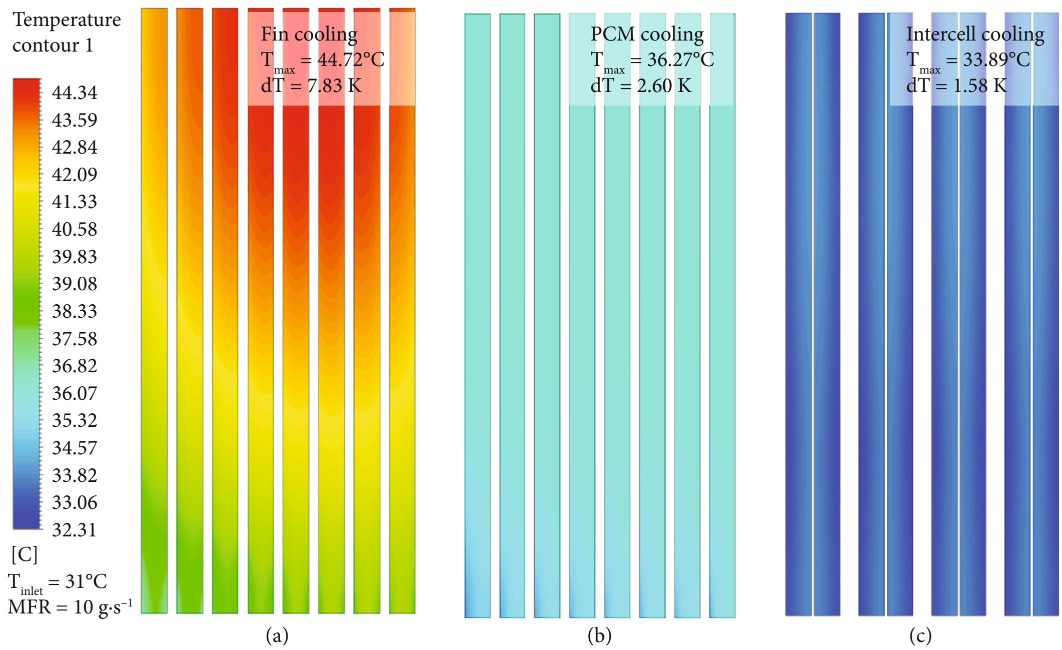

Figure 12: Temperature contours inside (a) fin, (b) PCM, and (c) intercell BTMSs with high inlet temperature (31°C).

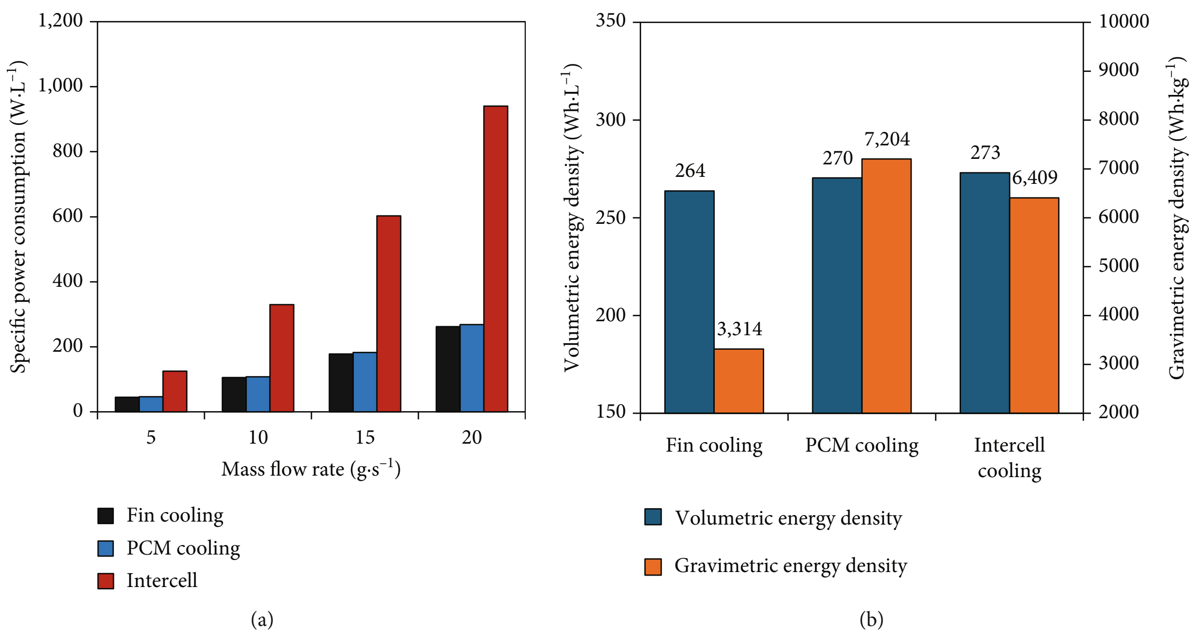

Figure 13: (a) Ideal power consumption and (b) energy density for each BTMS.

[38, 39], underscoring the impact of exceeding operational temperature limits on the acceleration of lithium-ion batteries' aging processes.

Conversely, low temperatures significantly impair lithium-ion battery performance, inducing degradation and capacity loss [29, 40, 41]. This performance degradation is attributed to a marked decrease in the solid-phase diffusion coefficient, which leads to concentration difference polarization and a swift drop to the cut-off voltage, thereby considerably diminishing the available capacity. Furthermore, a rise in charge transfer resistance signals decelerated electrochemical reaction rates, intensifying performance degradation in cold conditions. Additionally, electrolyte freezing in extremely cold conditions may result in discharge failure.

Challenges related to charging and discharging become pronounced, posing safety risks such as lithium dendrite formation, which can cause short circuits and thermal runaway during extreme temperature fluctuations. Thus, preheating or precooling batteries prior to charging or discharging is essential. This study explores the effects of precooling and preheating on battery thermal management, using three distinct systems.

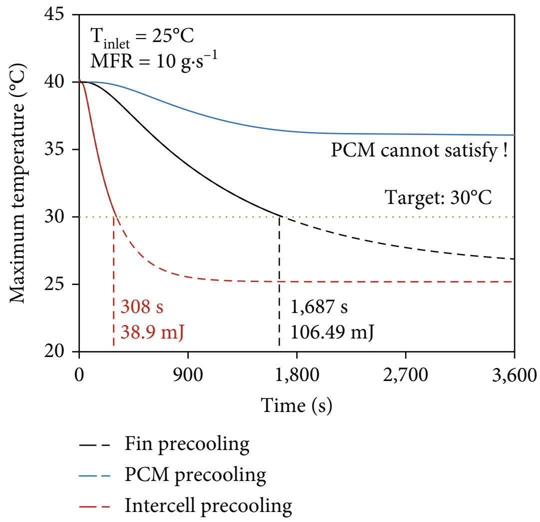

(a)

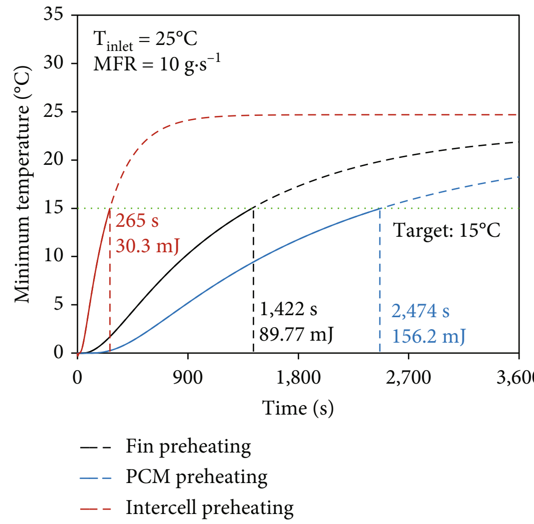

(b)

Figure 14: Performance of (a) precooling and (b) preheating of each BTMS.

In a high-temperature environment, with an initial and ambient temperature of 40°C, the study assessed how quickly the battery's maximum temperature could be reduced to 30°C as shown in Figure 14(a). With a coolant's mass flow rate set at 10 g•s^{-1} and inlet temperature at 25°C, results indicated that the fin-based thermal management system could reduce the maximum temperature to 30°C in 1,687 seconds. In contrast, the phase change material BTMS failed to achieve this even after 3,600 seconds due to its melting temperature of 36.1°C acting as a thermal barrier, thereby precluding temperature reduction before PCM solidification. Meanwhile, the intercell BTMS succeeded in lowering the battery temperature below 30°C in just 308 seconds, proving to be approximately 81.7% faster than fin cooling, with a significant reduction in power consumption by about 63.5%.

This study further evaluated the time required to increase the battery's minimum temperature to 15°C from an initial 0°C as shown in Figure 14(b). The fin BTMS needed 1,422 seconds, while the PCM BTMS took 2,474 seconds, hindered by the PCM's low thermal conductivity in its solid state, which impeded heat transfer. However, preheating via the intercell BTMS was significantly faster, achieving the target temperature in only 265 seconds, showcasing superior efficiency in diverse climatic conditions with reduced power consumption.

The preceding analysis underscores the fin BTMS's inadequate thermal performance at room temperature. Under varying climatic conditions, deploying a PCM-based thermal management system poses challenges due to its fixed melting point. Selecting an appropriate PCM type based on environmental conditions is crucial. Despite higher power consumption, the intercell BTMS, with reduced operating time, emerges as a highly efficient thermal management solution capable of addressing diverse climatic challenges.

5. Conclusions

In this study, the performances of three types of BTMSs were compared under various conditions, and the main conclusions were summarized as follows:

(i) The BTMSs were developed to enhance their thermal performances while maintaining a similar volume for each system. This involved using copper fins with high thermal conductivity for fin cooling, selecting an appropriate PCM thickness to provide sufficient latent heat for PCM cooling, and optimizing the plate design for intercell cooling

(ii) In the context of 3C charging, fin cooling did not meet the prescribed target temperature conditions, whereas PCM cooling successfully achieved the desired maximum temperature. However, PCM cooling struggled with an unacceptable temperature difference within the battery. In stark contrast, intercell cooling consistently met the desired temperature conditions, even at low flow rates

(iii) Increasing the coolant's inlet temperature effectively reduced the temperature difference between the upper and lower battery sections, resulting in reductions of 1.5 K and 4.3 K for fin cooling and PCM cooling, respectively, using the bottom cooling plate. However, fin cooling showed suboptimal thermal performance as its maximum temperature continued to rise, while PCM cooling successfully limited the maximum temperature. Conversely, increasing the coolant temperature did not positively affect intercell cooling

(iv) Despite intercell cooling demonstrating superior thermal performance, its specific power consumption was approximately three times higher than that of other methods. In terms of gravimetric energy density, fin cooling achieved only half the performance of other methods due to the use of heavy copper, whereas the PCM method exhibited approximately 12% better performance than intercell cooling

(v) In scenarios applying a precooling effect for high ambient temperatures, the intercell method required 81% less time and 63% less power (308 s and 38.9 mJ, respectively) to achieve the target temperature compared to the fin BTMS. However, the PCM BTMS, struggling with PCM solidification challenges, failed to reach the target temperature even after an hour. During preheating in low ambient temperatures, the intercell BTMS achieved the target temperature significantly faster and consumed less power than other methods, requiring 265 s and 30.3 mJ, respectively

The conventional battery thermal management system using fins was heavy and lacked the capacity for adequate thermal management; consequently, alternative methods needed to be considered. The intercell BTMS proved suitable in scenarios requiring robust thermal management, even if it involved higher power consumption across various temperature ranges. In contrast, the PCM BTMS was appropriate in situations where minimizing power consumption was crucial, especially in temperature ranges close to room temperature. Hence, selecting an appropriate BTMS could be based on specific target operating conditions.

Lithium-ion batteries come in various types, such as LCO, LMO, and LFP, categorized based on the battery material type. However, this classification pertains only to the material type, and the electrochemical reaction inside the battery remains consistent. Previous research indicates that the amount of heat generated by the battery changes in a similar order for different battery types [42]. Therefore, the results of the battery thermal management system in this study are expected to follow similar trends, although the specific values may vary slightly when applied to other commercially available batteries. This study is also anticipated to serve as a reference for determining the appropriate battery thermal management method, especially when considering faster battery charging conditions or developing an optimal battery thermal management system.

Appendix

Optimization

This study employed the OAAO technique to develop an optimal cooling plate for the intercell cooling system. The purpose of the intercell cooling plate optimization is to increase the thermal-hydraulic performance of the battery cooling plate by reducing the temperature difference between the battery and the pressure drop. The OAAO is a computational method that helps reduce the computational cost associated with numerical simulations and optimization algorithms [43]. A flow chart of the OAAO process is presented in Figure 15, and the main steps are conducted in the following order: (1) initial CFD simulation, (2) design of experiments, (3) parallel parameterized CFD, (4) meta model, and (5) optimization. The process before the meta model can be considered a preliminary step in building a training dataset for the meta model.

The preliminary work involved conducting an initial CFD simulation in which the user developed a 3D geometry model for analysis and parameterized it to generate various geometries. Because the optimization required a large amount of simulation data, 3D geometry modeling was simplified to reduce the computational cost. Only half of the battery module and intercell cooling system were designed, and symmetry was applied to the middle plane. The selected geometric parameters used as inputs for the meta model are shown in Figure 6(a). The initial and optimized parameters and their ranges utilized in the optimization process are listed in Table 6. After setting the input parameters, mesh generation and simulation were performed. The mesh structure was created in a tetrahedral form and converted into a polyhedral form in ANSYS Fluent. The boundary conditions were set in the simulation setup, and the numerical results were defined as the output parameters. The boundary and initial conditions were set as follows:

(i) Transient analysis during 3C fast-charging condition

(ii) Ambient and initial temperature: 25°C

(iii) Convection heat transfer coefficient: $2.3\,\mathrm{W{\bullet}m^{-2}{\bullet}K^{-1}}$

(iv) Type of coolant: water

(v) Inlet temperature of coolant: 25°C

(vi) Total mass flow rate: $10\,\mathrm{g{\bullet}s^{-1}}$

From the grid independence test, the element number of 581,160 was selected as the appropriate grid number because the maximum temperature and pressure drop converged. Compared to the element numbers of 348,006 and 700,249, the differences in the maximum temperature were 0.07% and -0.14%, respectively, and the differences in the pressure drop were 0.16% and -0.03%, respectively. After running the CFD simulation and verifying the grid independence, the next step was to establish the design of experiments (DOE), which involved setting the range of the input parameters and sampling them accordingly. The DOE was produced with 160 samples of channel shapes according to the changes in these geometric parameters. In this study, Latin hypercube sampling (LHS) was employed to distribute the samples uniformly along the parameter range with a smaller number of samplings. The sampled input parameters were then sent to the parallel parameterized CFD (PPCFD) step. The CFD simulations based on the initial settings were repeated for each sample, and the output results were exported to the DOE and recorded as the output dataset.

Once the DOE was filled with all the outputs, the data based on the DOE of the 160 samples were imported to develop a meta model. In this study, genetic aggregation

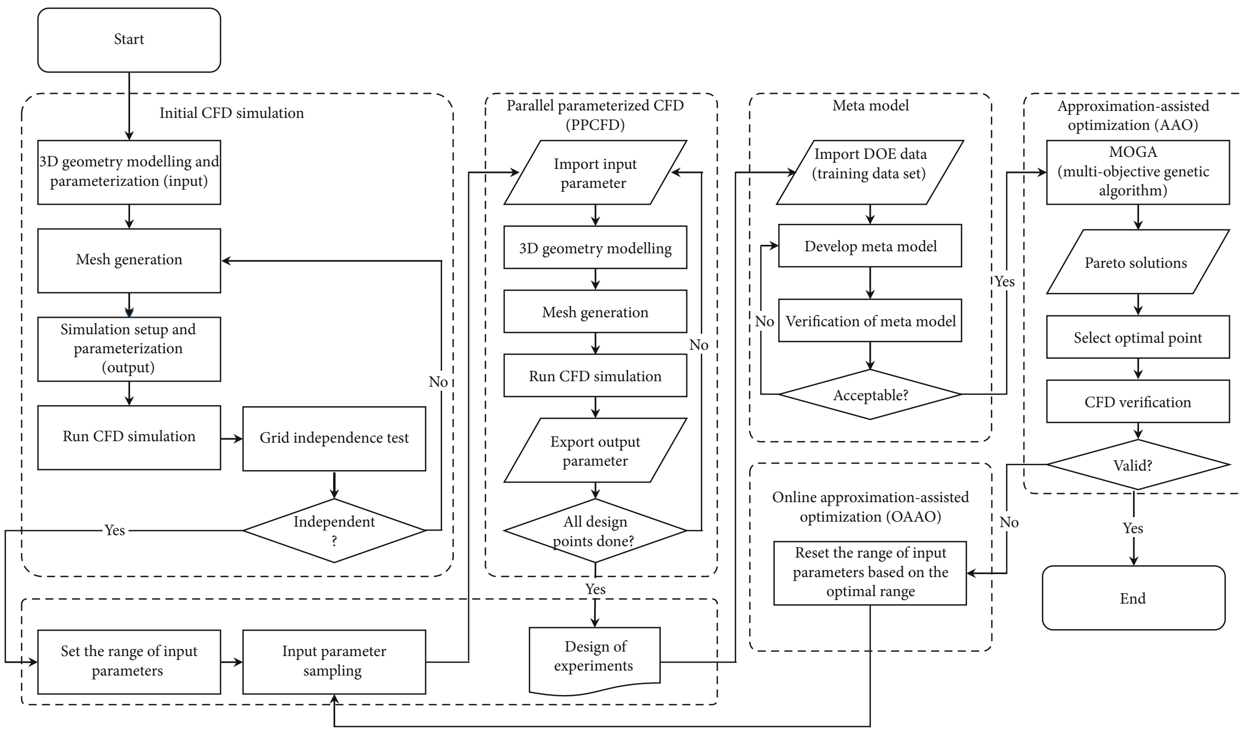

Figure 15: Flow chart of the multiobjective optimization using OAAO.

was used, as it automatically selects the most suitable meta model for each output among several options, including full 2nd-order polynomials, nonparametric regression, kriging, and moving least squares. The accuracy of the meta model was verified by comparing the output from the CFD simulations with the predictions of the meta model using another random sample. If the prediction error of the meta model is acceptable, the meta model can be used in the optimization algorithm. Twenty-five random verification points were generated to validate the results. Validation was conducted for the temperature difference and the pressure drop and was completed with an error within 5%.

This study employed a multiobjective genetic algorithm (MOGA) to determine the optimal point that satisfies both the minimum temperature difference in the battery module and the minimum pressure drop of the cooling plate. The combination of the meta model and optimization algorithm provided the Pareto solutions, which represented the combinations of optimal points that satisfy multiple objectives. Among the Pareto solutions, the optimal point can be selected based on certain criteria, and CFD verification was conducted to check for deviations from the true CFD results.

To reduce the computational time or improve the accuracy of deriving the optimal point, the OAAO method can be applied after the CFD verification. In this study, two further iterations of the optimization process were conducted, and the range of input parameters was reset along with the range of the Pareto solutions at each start of the OAAO. The accuracy of predicting the optimal model can be improved by maintaining the size of the DOE at 160 samples. After the third AAO, the optimal point was deemed valid, and an optimized cooling plate was developed. The optimized cooling plate design reduced the temperature difference and the pressure drop by 19.9% and 19.2%, respectively.

Nomenclature

Symbols

A: Heat transfer area (m^2)
Bi: Biot number
C_{mush}: Mush zone parameter
c_p: Specific heat ($J{\bullet}kg^{-1}{\bullet}K^{-1}$)
d: Diameter (m)
E: Energy (Wh)
f: Liquid fraction
$\vec{g}$: Gravitational vector ($m{\bullet}s^{-2}$)
h: Heat transfer coefficient ($W{\bullet}m^{-1}{\bullet}K^{-2}$)
h_{PCM}: Sensible enthalpy ($J{\bullet}kg^{-1}$)
h_{sl}: Latent heat ($J{\bullet}kg^{-1}$)
H: Specific enthalpy ($J{\bullet}kg^{-1}$)
I: Current (A)
k: Thermal conductivity ($W{\bullet}m^{-1}{\bullet}K^{-1}$)
L_c: Characteristic length (m)
m: Mass (kg)
$\dot{m}$: Mass flow rate ($kg{\bullet}s^{-1}$)
ΔP: Pressure drop (Pa)
∇P: Static pressure (Pa)
$\dot{Q}$: Heat (W)
R: Calculated parameter
Re: Reynolds number
t: Time (s)

T: Temperature (°C)
$\vec{v}$: Velocity vector (m•s^{-1})
V: Voltage (V)
Vol: Volume (m^3)
W: Power consumption (W)
x: Measured parameter
γ: Gravimetric energy density (Wh•kg^{-1})
δ: Volumetric energy density (Wh•m^{-3})
μ: Dynamic viscosity (kg•m^{-1}•s^{-1})
ρ: Density (kg•m^{-3}).

Abbreviations

3D: Three dimensional
BTMS: Battery thermal management system
CC: Constant current
CFD: Computational fluid dynamics
C-rate: Current rate (C)
CV: Constant voltage
DAQ: Data acquisition
DOE: Design of experiments
EPDM: Ethylene-propylene-diene rubber
EV: Electric vehicle
F.S: Full scale
ICEV: Internal combustion engine vehicle
LHS: Latin hypercube sampling
MFR: Mass flow rate
MOGA: Multiobjective genetic algorithm
OAAO: Online approximation-assisted optimization
OCV: Open-circuit voltage
PCM: Phase change material
PPCFD: Parallel parameterized computational fluid dynamics
RTD: Resistance temperature detector
SOC: State of charge
TC: Thermocouple.

Subscripts

amb: Ambient
bat: Battery
cell: Battery cell
dis: Dissipated
f: Fluid
gen: Generated
irr: Irreversible
max: Maximum
melting: Melting point
oc: Open circuit
pcm: Phase change material
ref: Reference
s: Solid
spe: Specific
x: x-direction
y: y-direction
z: z-direction.

Data Availability

Data will be made available based on the request.

Conflicts of Interest

The authors declare that they have no conflicts of interest.

Acknowledgments

This work was supported by the National Research Foundation of Korea (NRF) grant funded by the Korea government (MSIT) (No. RS-2023-00208700).

References

[1] H. Kim, J. Hong, H. Choi, J. Oh, and H. Lee, "Development of PCM-based shell-and-tube thermal energy storages for efficient EV thermal management," *International Communications in Heat and Mass Transfer*, vol. 154, article 107401, 2024.

[2] J. Hong, J. Song, U. Han, H. Kim, H. Choi, and H. Lee, "Performance investigation of electric vehicle thermal management system with thermal energy storage and waste heat recovery systems," *ETransportation*, vol. 20, article 100317, 2024.

[3] W. Cheng, M. Chen, D. Ouyang, J. Weng, L. Zhao, and Y. Chen, "Investigation of the thermal performance and heat transfer characteristics of the lithium-ion battery module based on an oil-immersed cooling structure," *Journal of Energy Storage*, vol. 79, article 110184, 2024.

[4] M. Chen, W. Cheng, L. Zhao, and Y. Chen, "Feasibility study and dimensionless theoretical analysis of cylindrical lithium-ion battery module cooled by dynamic circulating transformer oil," *Applied Thermal Engineering*, vol. 236, article 121737, 2024.

[5] U. Han, Y. J. Jun, H. Choi, and H. Lee, "Thermal performance analysis and optimization of heat pipe-assisted hybrid fin structure for lithium battery thermal management for extreme thermal conditions," *International Communications in Heat and Mass Transfer*, vol. 149, article 107128, 2023.

[6] H. Choi, J. Hong, S. Lee, D. Kim, and H. Lee, "A novel battery thermal management system for cooling/preheating utilizing a polymer intercell heat exchanger with phase change material," *Applied Thermal Engineering*, vol. 238, article 122248, 2024.

[7] A. K. Thakur, M. S. Ahmed, H. Kang et al., "Critical review on internal and external battery thermal management systems for fast charging applications," *Advanced Energy Materials*, vol. 13, no. 11, pp. 1–37, 2023.

[8] G. Zhao, X. Wang, M. Negnevitsky, and C. Li, "An up-to-date review on the design improvement and optimization of the liquid-cooling battery thermal management system for electric vehicles," *Applied Thermal Engineering*, vol. 219, article 119626, 2023.

[9] H. Choi, U. Han, and H. Lee, "Effects of diverging channel design cooling plate with oblique fins for battery thermal management," *International Journal of Heat and Mass Transfer*, vol. 200, article 123485, 2023.

[10] T. Wang, X. Zhang, Q. Zeng, K. Gao, and S. Jiang, "Bidirectional heat transfer characteristics of cavity cold plate battery thermal management system: an experimental study," *Applied Thermal Engineering*, vol. 225, article 120242, 2023.

[11] K. Yang, Z. Ling, X. Fang, and Z. Zhang, "Introducing a flexible insulation network to the expanded graphite-based composite phase change material to enhance dielectric and mechanical properties for battery thermal management," *Journal of Energy Storage*, vol. 66, article 107486, 2023.

[12] L. K. Singh, R. Kumar, A. K. Gupta, A. K. Sharma, and S. Panchal, "Computational study on hybrid air-PCM cooling inside lithium-ion battery packs with varying number of cells," *Journal of Energy Storage*, vol. 67, article 107649, 2023.

[13] Z. Liu, X. Liu, H. Meng, L. Guo, and Z. Zhang, "Numerical analysis of the thermal performance of a liquid cooling battery module based on the gradient ratio flow velocity and gradient increment tube diameter," *International Journal of Heat and Mass Transfer*, vol. 175, article 121338, 2021.

[14] H. Choi, H. Lee, J. Kim, and H. Lee, "Hybrid single-phase immersion cooling structure for battery thermal management under fast-charging conditions," *Energy Conversion and Management*, vol. 287, article 117053, 2023.

[15] A. Khan, S. Yaqub, M. Ali et al., "A state-of-the-art review on heating and cooling of lithium-ion batteries for electric vehicles," *Journal of Energy Storage*, vol. 76, article 109852, 2024.

[16] Y. Chung and M. S. Kim, "Thermal analysis and pack level design of battery thermal management system with liquid cooling for electric vehicles," *Energy Conversion and Management*, vol. 196, pp. 105–116, 2019.

[17] J. Xie, Y. Wang, S. He, G. Zhang, X. Liu, and X. Yang, "A simple cooling structure with precisely-tailored liquid cooling plate for thermal management of large battery module," *Applied Thermal Engineering*, vol. 212, article 118575, 2022.

[18] Z. Feng, J. Zhao, C. Guo et al., "Optimization of the cooling performance of symmetric battery thermal management systems at high discharge rates," *Energy & Fuels*, vol. 37, no. 11, pp. 7990–8004, 2023.

[19] S. Gungor, E. Cetkin, and S. Lorente, "Canopy-to-canopy liquid cooling for the thermal management of lithium-ion batteries, a constructal approach," *International Journal of Heat and Mass Transfer*, vol. 182, article 121918, 2022.

[20] A. Kumar Thakur, R. Sathyamurthy, R. Velraj et al., "A state-of-the art review on advancing battery thermal management systems for fast-charging," *Applied Thermal Engineering*, vol. 226, article 120303, 2023.

[21] S. Lee, U. Han, and H. Lee, "Development of a hybrid battery thermal management system coupled with phase change material under fast charging conditions," *Energy Conversion and Management*, vol. 268, article 116015, 2022.

[22] W. Dai and H. Lai, "Comparative study of flow-channel layout schemes in liquid cooling plates of a prismatic battery module," *Applied Thermal Engineering*, vol. 236, article 121501, 2024.

[23] J. Liu, H. Chen, M. Yang, S. Huang, and K. Wang, "Comparative study of natural ester oil and mineral oil on the applicability of the immersion cooling for a battery module," *Renewable Energy*, vol. 224, article 120187, 2024.

[24] J. Xu, Z. Guo, Z. Xu, X. Zhou, and X. Mei, "A systematic review and comparison of liquid-based cooling system for lithium-ion batteries," *ETransportation*, vol. 17, article 100242, 2023.

[25] R. D. Jilte, R. Kumar, M. H. Ahmadi, and L. Chen, "Battery thermal management system employing phase change material with cell-to-cell air cooling," *Applied Thermal Engineering*, vol. 161, article 114199, 2019.

[26] X. Wu, Z. Zhu, H. Zhang, S. Xu, Y. Fang, and Z. Yan, "Structural optimization of light-weight battery module based on hybrid liquid cooling with high latent heat PCM," *International Journal of Heat and Mass Transfer*, vol. 163, article 120495, 2020.

[27] U. Han, S. Lee, Y. J. Jun, and H. Lee, "Experimental investigation on thermal performance of battery thermal management system with heat pipe assisted hybrid fin structure under fast charging conditions," *Applied Thermal Engineering*, vol. 230, article 120840, 2023.

[28] X. Xu, J. Zhu, H. Zhang, Z. Yi, X. Wang, and G. Zhao, "Low cost energy-efficient preheating of battery module integrated with air cooling based on a heat spreader plate," *Applied Thermal Engineering*, vol. 232, article 121024, 2023.

[29] S. Wu, R. Xiong, H. Li, V. Nian, and S. Ma, "The state of the art on preheating lithium-ion batteries in cold weather," *Journal of Energy Storage*, vol. 27, article 101059, 2020.

[30] D. Chen, J. Jiang, G. H. Kim, C. Yang, and A. Pesaran, "Comparison of different cooling methods for lithium ion battery cells," *Applied Thermal Engineering*, vol. 94, pp. 846–854, 2016.

[31] U. Golla-Schindler, D. Zeibig, L. Prickler, S. Behn, T. Bernthaler, and G. Schneider, "Characterization of degeneration phenomena in lithium-ion batteries by combined microscopic techniques," *Micron*, vol. 113, pp. 10–19, 2018.

[32] U. Han, H. Kang, J. Song, J. Oh, and H. Lee, "Development of dynamic battery thermal model integrated with driving cycles for EV applications," *Energy Conversion and Management*, vol. 250, article 114882, 2021.

[33] S. Mousavi, A. Zadehkabir, M. Siavashi, and X. Yang, "An improved hybrid thermal management system for prismatic Li-ion batteries integrated with mini-channel and phase change materials," *Applied Energy*, vol. 334, article 120643, 2023.

[34] B. Zirnstein, D. Schulze, and B. Schartel, "Mechanical and fire properties of multicomponent flame retardant EPDM rubbers using aluminum trihydroxide, ammonium polyphosphate, and polyaniline," *Materials*, vol. 12, no. 12, pp. 1–22, 2019.

[35] U. Han, J. Kim, H. Choi, H. Lee, and H. Lee, "Inverse heat transfer analysis method to determine the entropic coefficient of reversible heat in lithium-ion battery," *International Journal of Energy Research*, vol. 2023, Article ID 9929496, 18 pages, 2023.

[36] N. Yang, X. Zhang, G. Li, and D. Hua, "Assessment of the forced air-cooling performance for cylindrical lithium-ion battery packs: a comparative analysis between aligned and staggered cell arrangements," *Applied Thermal Engineering*, vol. 80, pp. 55–65, 2015.

[37] U. Han, H. Kang, H. Lim, J. Han, and H. Lee, "Development and design optimization of novel polymer heat exchanger using the multi-objective genetic algorithm," *International Journal of Heat and Mass Transfer*, vol. 144, article 118589, 2019.

[38] A. K. Thakur, R. Prabakaran, M. R. Elkadeem et al., "A state of art review and future viewpoint on advance cooling techniques for lithium–ion battery system of electric vehicles," *Journal of Energy Storage*, vol. 32, article 101771, 2020.

[39] M. Lu, X. Zhang, J. Ji, X. Xu, and Y. Zhang, "Research progress on power battery cooling technology for electric vehicles," *Journal of Energy Storage*, vol. 27, article 101155, 2020.

[40] Y. Wang, X. Zhang, and Z. Chen, "Low temperature preheating techniques for lithium-ion batteries: recent advances and future challenges," *Applied Energy*, vol. 313, article 118832, 2022.

[41] Y. Wang, Z. Chen, and C. Zhang, "On-line remaining energy prediction: a case study in embedded battery management system," *Applied Energy*, vol. 194, pp. 688–695, 2017.

[42] A. Nazari and S. Farhad, "Heat generation in lithium-ion batteries with different nominal capacities and chemistries," *Applied Thermal Engineering*, vol. 125, pp. 1501–1517, 2017.

[43] S. Wang, G. Jian, J. Xiao, J. Wen, and Z. Zhang, "Optimization investigation on configuration parameters of spiral-wound heat exchanger using genetic aggregation response surface and multi-objective genetic algorithm," *Applied Thermal Engineering*, vol. 119, pp. 603–609, 2017.